

AMERICAN UNIVERSITY OF BEIRUT

PERIPROSTATIC ADIPOSE TISSUE  
THROMBOINFLAMMATION DRIVES EARLY  
NEOPLASTIC ALTERATIONS IN A RAT MODEL OF MILD  
METABOLIC DYSFUNCTION

by  
IBRAHIM MOHAMAD ALZAIM

A thesis  
submitted in partial fulfillment of the requirements  
for the degree of Master of Science  
to the Department of Biochemistry and Molecular Genetics  
of the Faculty of Medicine  
at the American University of Beirut

Beirut, Lebanon  
June 2022

AMERICAN UNIVERSITY OF BEIRUT

PERIPROSTATIC ADIPOSE TISSUE  
THROMBOINFLAMMATION DRIVES EARLY  
NEOPLASTIC ALTERATIONS IN A RAT MODEL OF MILD  
METABOLIC DYSFUNCTION

by  
IBRAHIM MOHAMAD ALZAIM

Approved by:



---

Dr. Nadine Darwiche, Professor  
Department of Biochemistry and Molecular Genetics

Advisor



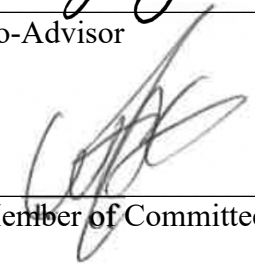
---

Dr. Ahmed Fawzi El-Yazbi, Professor  
Department of Pharmacology and Experimental Therapeutics

Co-Advisor

---


Dr. Wassim Abou-Kheir, Associate Professor  
Department of Anatomy, Cell Biology, and Physiology



Member of Committee

---

Dr. Firas Kobeissy, Associate Professor  
Department of Biochemistry and Molecular Genetics



Member of Committee

Date of thesis defense: June 30, 2022

# AMERICAN UNIVERSITY OF BEIRUT

## THESIS RELEASE FORM

Student Name: AlZaim Ibrahim Mohamad  
Last First Middle

I authorize the American University of Beirut, to: (a) reproduce hard or electronic copies of my thesis; (b) include such copies in the archives and digital repositories of the University; and (c) make freely available such copies to third parties for research or educational purposes:

- As of the date of submission
- One year from the date of submission of my thesis.
- Two years from the date of submission of my thesis.
- Three years from the date of submission of my thesis.



September 09, 2022

Signature

Date

## ACKNOWLEDGEMENTS

I would first like to express my sincere gratitude to my advisor Dr. Nadine Darwiche for her support and guidance throughout my research journey as a graduate student at AUB.

Also, I would like to wholeheartedly thank my mentor, co-advisor, and good friend Dr. Ahmed F. El-Yazbi for his support, guidance, and motivation that extend beyond my graduate studies.

I would also like to thank Dr. Wassim Abou Kheir for his continuous support, mentorship, and kindness.

My sincere thanks also go to my committee member Dr. Firas Kobeissy for his critical comments.

I would also like to thank all my fellow lab members, particularly Ms. Nahed Mougharbil, Dr. Rana Alaaeddine, and Ms. Aya Al-Saidi for their kindness and support extending beyond the work depicted in the submitted thesis.

# ABSTRACT OF THE THESIS OF

Ibrahim Mohamad AlZaim

for

Master of Science

Major: Biochemistry

Title: Periprostatic Adipose Tissue Thromboinflammation Drives Early Neoplastic Alterations in a Rat Model of Mild Metabolic Dysfunction

Emerging evidence links periprostatic adipose tissue (PPAT) inflammation, a consequence of metabolic impairment, to certain features of prostate cancer (PCa) aggressiveness. AT thromboinflammation, mediated by the proteolytic activation of protease-activated receptors (PARs) particularly thrombin and Factor Xa (FXa), drives AT dysfunction. Nevertheless, the contribution of PPAT thromboinflammation to the early prostatic neoplastic alterations associated with mild metabolic impairment have not been investigated. Here, we utilized a non-obese prediabetic rat model to assess prostatic neoplasia in association with PPAT thromboinflammation. Mild hypercaloric diet (MHC)-fed rats exhibited hyperinsulinemia, insulin resistance, hypertriglyceridemia, a lower metabolic efficiency, and a higher fat/lean ratio in comparison to regular chow-fed rats. When compared to regular chow-fed rats, MHC-fed rats exhibited PPAT with hypertrophied adipocytes, enhanced oxidative stress, and increased proinflammatory macrophage infiltration. Particularly, PPAT of MHC-fed rats exhibited enhanced fibrin deposition indicative of increased PPAT FXa activity. Concurrently, prostates from MHC-fed rats displayed a higher number of prostatic intraepithelial neoplasia (PIN), pronounced fibrosis, increased proinflammatory macrophage influx, and enhanced expression of hyperproliferative and epithelial-to-mesenchymal (EMT) markers. Importantly, these prostatic and adipocytic manifestations were attenuated in MHC-fed rats treated with a non-hemorrhagic dose of rivaroxaban, a direct FXa inhibitor. Furthermore, we investigated the possible direct effects of rivaroxaban on murine Plum-AD androgen-dependent *Pten*<sup>-/-</sup> *p53*<sup>-/-</sup> prostatic epithelial cancer cells *in vitro*. Rivaroxaban inhibited Plum-AD proliferation, migration, and colony formation, in addition to enhancing oxidative stress. While the anti-proliferative effect can be explained by rivaroxaban-mediated inhibition of PAR-2 signaling, rivaroxaban-mediated inhibition of Plum-AD migration, and colony formation seems to be independent of PAR-2 signaling. As such, further investigation is required to delineate the molecular underpinnings of rivaroxaban-associated amelioration of PPAT thromboinflammation and the associated prostatic neoplastic alterations secondary to metabolic dysfunction.

## TABLE OF CONTENTS

ACKNOWLEDGEMENTS .....	1
ABSTRACT .....	2
ILLUSTRATIONS.....	5
INTRODUCTION .....	9
A. Periprostatic Adipose Tissue: An Under-studied Adipose Depot at the Nexus of Metabolic Dysfunction and Prostate Cancer.....	9
B. Molecular Particularities of the Periprostatic Adipose Tissue.....	10
C. Periprostatic Adipose Tissue: A Microenvironmental Contributor to Prostate Cancer .....	11
D. Metabolic Syndrome, Obesity, and Prostate Cancer: States of Hypercoagulability .....	13
E. Thromboinflammatory Processes Drive Adipose Tissue Inflammation.....	15
OBJECTIVE, SPECIFIC AIMS, AND SIGNIFICANCE.....	17
MATERIALS AND METHODS.....	18
A. Animal Model and Experimental Design.....	18
B. Random Blood Glucose Measurement and Intraperitoneal Glucose and Insulin Tolerance Tests .....	19
C. Noninvasive Hemodynamics, Body Composition, Organ Harvest, Serum Collection, and Serum Analysis.....	19
D. Histopathology, Immunohistochemistry, and Immunofluorescence .....	20

E. Determination of Macrophage Polarization by Fluorescence-Activated Cell Sorting .....	24
F. Cell Culture .....	25
G. Cell Proliferation, Cell Growth Inhibition, and Cell Viability Assays .....	26
H. Cell Cycle Analysis .....	28
I. Assessment of Cellular Oxidative Stress .....	28
J. Assessment of Mitochondrial Membrane Potential .....	29
K. Cell Migration Assay .....	30
L. Colony Formation Assay.....	30
M. Statistical Analysis .....	31
<b>RESULTS .....</b>	<b>32</b>
A. Metabolic Consequences of Mild Hypercaloric Diet Consumption .....	32
B. Periprostatic Adipose Tissue Dysfunction is a Hallmark of Prediabetes.....	34
C. Periprostatic Adipose Tissue Dysfunction is Associated with Early Prostatic Neoplastic Alterations in Prediabetes .....	37
D. Protease-activated Receptor 2 Agonism Modulates Rivaroxaban Effects on Prostate Cancer Cells <i>in vitro</i> .....	41
<b>DISCUSSION .....</b>	<b>45</b>
<b>LIMITATIONS AND FUTURE DIRECTIONS .....</b>	<b>50</b>
<b>REFERENCES.....</b>	<b>51</b>

## ILLUSTRATIONS

### Figure

1. Metabolic consequences of Mild Hypercaloric Diet Consumption. ....33
2. Periprostatic adipose tissue expansion is a hallmark of prediabetes.....34
3. Rivaroxaban modulates metabolic dysfunction-driven periprostatic adipose tissue thromboinflammation.....35
4. Periprostatic adipose tissue exhibits no pro-fibrotic or pro-thermogenic phenotype in prediabetes.....37
5. Rivaroxaban modulates early prostatic neoplastic alterations secondary to mild metabolic dysfunction. ....38
6. Rivaroxaban modulates prostatic tissue remodeling and inflammation secondary to metabolic dysfunction. ....39
7. Rivaroxaban ameliorates metabolic impairment-associated prostatic epithelial hyperproliferation and epithelial-to-mesenchymal transition. ....41
8. PAR-2 agonism mitigates rivaroxaban-induced cytotoxicity in cultured murine Plum-AD prostate cancer cells.....43
9. PAR-2 agonism does not reverse rivaroxaban-induced inhibition of Plum-AD cell migration and colony formation .....44



## ABBREVIATIONS

$\alpha$ -SMA, alpha smooth muscle actin

Akt, Protein kinase B

AT, Adipose tissue,

$\beta_3$ -AR, Beta-3 adrenergic receptor

BMI, Body mass index

BSA, Bovine serum albumin

CCL, C-C motif chemokine ligand

CCR, C-C motif chemokine receptor

CD, Cluster of differentiation

CK, Cytokeratin

CLS, Crown-like structure

CXCL, CXC motif chemokine ligand

CXCR, CXC motif chemokine receptor

DHE, Dihydroethidium

DIO, Diet-induced obesity

DMEM, Dulbecco's modified eagle medium

DMSO, Dimethyl sulfoxide

EGF, Epidermal growth factor

EMT, Epithelial to mesenchymal transition

FACS, Fluorescence-associated cell sorting

FBS, Fetal bovine serum

FXa, Active factor X

HFD, High fat diet

HIF, Hypoxia-inducible factor

IL, Interleukin

IpGTT, Intraperitoneal glucose tolerance test

IpITT, Intraperitoneal insulin tolerance test

IR, Insulin resistance

LDL, Low density lipoprotein

MCP1, Monocyte chemoattractant protein-1

MetS, Metabolic syndrome

MHC, Mild hypercaloric

MMP, Matrix metalloproteinase

MTT, 3-(4,5-dimethylthiazol-2-yl)-2,5-diphenyltetrazolium bromide

NBT, Nitroblue tetrazolium

NGS, Normal goat serum

NMR, Nuclear magnetic resonance

NOX, NADPH oxidase

PAI-1, Plasminogen activator inhibitor-1

PAR, Protease-activated receptor

PBS, Phosphate-buffered saline

PCa, Prostate cancer

PCNA, Proliferating cell nuclear antigen

PI, Propidium iodide

PIN, Prostatic intraepithelial neoplasia

PPAR, Peroxisome proliferator-activated receptor

PPAT, Periprostatic adipose tissue

ROS, Reactive oxygen species

SAT, Subcutaneous adipose tissue

SBP, Systolic blood pressure

SRB, Sulforhodamine B

TCA, Trichloroacetic acid

TF, Tissue factor

TFPI, Tissue factor pathway inhibitor

TGF, Transforming growth factor

TH, Tyrosine hydroxylase

TNF- $\alpha$ , Tumour necrosis factor

VAT, Visceral adipose tissue

VEGF, Vascular endothelial growth factor

VP, Ventral prostate

VWF, Von Willebrand factor

# CHAPTER I

## INTRODUCTION

### **A. Periprostatic Adipose Tissue: An Under-studied Adipose Depot at the Nexus of Metabolic Dysfunction and Prostate Cancer**

Despite a long-term decline in prostate cancer (PCa) patient mortality, PCa currently represents one of the leading cancers in men in terms of incidence, morbidity, and mortality (1). This is mirrored by an increased global prevalence and augmented economic burden of metabolic diseases including insulin resistance (IR), metabolic syndrome (MetS), obesity, and diabetes, which represent states of chronic low-grade inflammation (2, 3). Although seemingly distinct, accumulating evidence highlights associations between metabolic disturbances, particularly those culminating in obesity, and PCa development, progression, and worse prognosis (4). Such associations are underpinned by several factors, the most prominent of which is adipose tissue (AT) inflammation and the disruption of metabolic homeostasis. AT expansion, ensuing secondary to an imbalance between energy acquisition and energy expenditure, drives hyperinsulinemia and IR (5, 6). The diametric expansion of hypertrophied adipocytes beyond the diffusion potential of oxygen precipitates localized hypoxia in the absence of compensatory angiogenesis (7, 8). This hypoxic state results in adipocytic death, proinflammatory cytokines and chemokines production, and immune cell infiltration, the most prominent of which being macrophages forming crown-like structures (CLS) around apoptotic adipocytes (9). Single cell transcriptomic analysis identified marked AT cellular heterogeneity across adipose depots and differential insulin sensitivity across adipocytes belonging to the same adipose depot (10-13). Such an extensive heterogeneity

results in the emergence of a differential, depot-specific susceptibility to inflammation (9). Ample evidence links increased visceral adiposity to a worse prognosis of PCa. Nevertheless, the molecular underpinnings of such an association have not been fully elucidated. Periprostatic AT (PPAT) represents an understudied microenvironmental contributor to the development, progression, response to chemotherapy, and prognosis of PCa (14-17).

### **B. Molecular Particularities of the Periprostatic Adipose Tissue**

Research into high resolution cellular characterization of periprostatic adipocytes is lacking and the cellular heterogeneity of PPAT as well as its thermogenic potential remain largely uninvestigated. PPAT has been considered a visceral AT (VAT) despite its extraperitoneal localization. However, an extensive comparison between PPAT, VAT, and subcutaneous AT (SAT) depots has not been conducted. PPAT covers the subperitoneal region and is boarded by the anteriorpubic symphysis, the lateral obturator muscles, and the posterior rectoprostatic fascia (18). Although PPAT shares common vasculature and sympathetic innervation with the prostate, they are separated by a fibromuscular capsule (19-21). Nevertheless, one-third of the prostate anterior is in direct contact with the surrounding AT (18, 22). This proximal localization allows for profound crosstalk by which PPAT dysfunction, as a result of metabolic impairment, possibly contributes to neoplastic alterations of the healthy prostate and enhances the aggressiveness of PCa. In comparison to subcutaneous adipocytes, periprostatic adipocytes are smaller and are more sensitive to isoproterenol-stimulated lipolysis (23). Additionally, PPAT was shown to have a higher content of adipose-derived stem cells in comparison to VAT (24). Recent evidence suggests that in comparison with the

abdominopelvic AT, PPAT exhibits an intrinsically hypoxic phenotype that associates with PPAT inflammation and fibrosis, which are not upregulated by obesity (25).

### **C. Periprostatic Adipose Tissue: A Microenvironmental Contributor to Prostate Cancer**

Correlations between PPAT thickness/volume and body mass index (BMI) have yielded inconsistent results, likely owing to the fact that BMI does not represent a qualitative indicator of body composition or metabolic health and does not discriminate between visceral and subcutaneous adiposity (26). It is therefore evident that the inflammatory status of the PPAT rather than its dimensional measurements should be accounted for when assessing its correlation with PCa-associated parameters. As epidemiological and clinical studies implicate increased adiposity in driving PCa development, progression, and metastasis, investigation into inflammatory processes underpinning PPAT inflammation becomes essential, particularly with the accumulating evidence of hypercaloric diet-induced prostatic intraepithelial neoplasia (PIN) and PCa mainly through the activation of inflammatory processes (27, 28).

PPAT inflammation, evidenced by increased CLS formation, has been documented in PCa patients and was shown to associate with higher BMI, larger adipocytes, and higher Gleason grade (29). PPAT inflammation also correlated with higher levels of circulating insulin, triglycerides, and leptin, which are prominent hallmarks of the MetS. Murine models of diet-induced obesity (DIO) exhibit pronounced PPAT inflammation secondary to AT expansion, evidenced by the augmented expression of the macrophage marker CD68, the formation of CLS, and the expression of the proinflammatory cytokines MCP1 and TNF- $\alpha$  (30, 31). The modulation of PPAT inflammation through antidiabetic agents such as pioglitazone, a PPAR $\gamma$  agonist, in obese

mice reduced CLS density in PPAT and suppressed the expression of TNF- $\alpha$ , TGF- $\beta$ , and MCP-1 while upregulating the expression of the adipocytokine adiponectin (30). Moreover, other interventions including caloric restriction and the supplementation of 17 $\beta$ -estradiol were shown to reduce PPAT inflammation in DIO mice (31). Although these effects were primarily attributed to a reduction in food intake and to a marked weight loss, this does not exclude direct effects of estrogen on the PPAT.

Obese PPAT-conditioned media has been shown to enhance PCa cell proliferation and migration *in vitro* (32). Indeed, PPAT adipocytes were shown to direct PCa cells migration in an obesity-dependent manner (33, 34). PPAT adipocytes secrete CCL7/CXCL12 which diffuses to the peripheral zones of the prostate, stimulating the migration of CCR3-expressing and CXCR4/CXCR7-expressing tumor cells. This extraprostatic extension of PCa into PPAT has been suggested to be a more important determinant of PCa recurrence in comparison to an invasive phenotype (35). PCa lipophagy was also suggested to be associated with disease aggressiveness and correlates with the proximity of the PPAT (36). As such, tumor cells were shown to induce adipocyte lipolysis and the released free fatty acids stimulated tumor cell invasion through the upregulation of the NADPH oxidase NOX5 (37). NOX5-induced reactive oxygen species (ROS) activates the HIF1/MMP14 signaling axis, which is responsible for the enhanced tumor cell invasion. PPAT secreted TGF- $\beta$  is also suggested to drive PCa cell migration (38). These findings suggest pivotal roles for PPAT dysfunction in driving PCa cell migration.

Despite ample evidence of obesity-associated PPAT inflammation-induced promotion of PCa, cancerous hallmarks of murine xenografts of patient-derived, moderate-grade localized PCa were not altered by obesity in high fat diet (HFD)-fed mice

(39). Although coculture systems of stromal and epithelial cells demonstrated a pro-tumorigenic effect of human PPAT-secreted factors, co-grafting human PPAT with PCa in patient-derived xenograft mice revealed no tumorigenic acceleration in comparison to the PCa graft alone (39). These findings prompt the requirement for further investigation into the mechanisms by which increased adiposity, metabolic dysfunction, and obesity promote PCa in light of PPAT dysfunction.

#### **D. Metabolic Syndrome, Obesity, and Prostate Cancer: States of Hypercoagulability**

Metabolic syndrome is frequently accompanied by a prothrombotic state that is reflected by AT dysfunction and by alterations in the components of the coagulation system (40). Molecular pathways of coagulation have been reviewed elsewhere (40). Indeed, obesity increases the risk of venous thromboembolism secondary to increased thrombin generation, decreased fibrinolysis, and enhanced platelet hypercoagulability (41). Substantial clinical evidence emphasizes elevated levels of circulating Von Willebrand factor (vWF), tissue factor (TF), thrombin, FVII, FVIII, and fibrinogen in addition to increased levels of plasminogen activator inhibitor-1 (PAI-1) and thrombin activatable fibrinolysis inhibitor (TAFI) in obese subjects (26, 40, 42). Moreover, increased visceral adiposity has been suggested as an independent determinant of hypercoagulability in morbidly obese patients, as well as an instigator of shortened blood coagulation times in genetically-induced and diet-induced obesity animal models (43, 44). Likewise, central obesity in MetS patients is associated with increased circulating levels of FVII but with no alteration in the levels of antithrombin (45). However, inconsistent and conflicting data is reported concerning coagulation inhibitors. While chronic inflammation and IR are correlated with higher levels of fibrinogen and fibrin



formation reflecting impaired fibrinolysis (46, 47), levels of TF pathway inhibitor (TFPI) were found to be either increased or unaltered in patients with MetS (48). Importantly, AT represents a major source of TF, which levels are upregulated in states of low-grade inflammation (49, 50). Obese mice exhibit increased TF activity in adipocytes and adipose-infiltrating macrophages (51, 52). Moreover, weight loss in obese patients with MetS is associated with a significant reduction in the thrombin generation potential and circulating levels of soluble TF and FVII (53, 54). Consistent with clinical observations, caloric restriction and weight loss in obese mice decrease circulating levels of FVII and AT inflammation (55).

Cancer creates a highly prothrombotic state that is evidenced by cancer-associated venous thromboembolic events representing a major cause of morbidity and mortality in patients with malignancy (56), to counteract which, anticoagulants are frequently incorporated into the treatment guidelines of cancer patients (57, 58). Moreover, components of the hemostatic system are implicated in the early neoplastic alterations pivotal for tumorigenesis and tumor growth, cancer progression, and cancer metastasis (59). This is supported by studies providing evidence that chronic conventional anticoagulation is associated with a decreased incidence of certain cancers (60, 61). The direct effects of components of the coagulation cascade, particularly thrombin, and its downstream proteolytic substrates in PCa have been reviewed elsewhere and extend beyond the realm of our current focus (59). Importantly, it was shown that prostatic epithelial and stromal cells express thrombin, the generation level and procoagulant activity of which are associated with more advanced disease and worse prognosis of PCa (62). Thrombin is a protease possessing a myriad of substrates including PAR-1, PAR-2, and PAR-4 in addition to its hemostatic substrate, fibrinogen (63). Indeed, the enhanced

generation of thrombin in metabolic diseases is thought to drive neoplastic changes in the healthy prostate, at least in part, through its activity on PARs.

### **E. Thromboinflammatory Processes Drive Adipose Tissue Inflammation**

The pleiotropic activities of coagulation factors extending beyond coagulation are thought to drive metabolic dysfunction through their activities on metabolically active tissues including the AT (42). Indeed, extravascular fibrin deposits were identified in white AT of HFD-fed mice and obese individuals, indicative of enhanced AT thrombin activity and reduced fibrinolysis (64). Mice carrying a mutant form of fibrinogen that is incapable of binding to the leukocyte  $\alpha M\beta 2$ -integrin were not only resistant to DIO, but also had significantly diminished AT inflammation evidenced by reduced macrophage infiltration (64). Contrastingly, homozygous thrombomodulin mutant mice, characterized by an elevated procoagulant activity of thrombin, exhibited a more pronounced DIO phenotype (64). Consistently, *in vitro* studies demonstrated that thrombin increases adipocyte secretion of the proinflammatory cytokines IL-1 $\beta$ , IL-6, MCP-1, and TNF- $\alpha$ , along with the growth factor vascular endothelial growth factor (VEGF) (65). As such, the pharmacological inhibition of thrombin activity with the direct thrombin inhibitor dabigatran was shown to limit the development of obesity in DIO mice (64, 66). Moreover, inhibiting thrombin activity with dabigatran decreased proinflammatory cytokines production in HFD-fed female LDL receptor-deficient mice and decreased M1 macrophage polarization without significantly reducing adipocyte hypertrophy (67). Similarly, argatroban administration to db/db obese diabetic mice was shown to reduce fasting plasma glucose and enhance insulin sensitivity (68). Argatroban treatment also reduced adipocyte size, macrophage infiltration, and the expression of MCP-1, IL-6, and

FVII in the AT (68). Indeed, the enhanced adiposity-induced, FVII-mediated generation of thrombin is thought to drive AT insulin resistance and macrophage infiltration. It is worth mentioning that TNF- $\alpha$  and  $\beta$ -adrenoreceptor agonism stimulates FVII secretion from adipocytes via the cyclic AMP/PKA pathway (69). TF mediates the FVIIa-dependent activation of PAR-2, which was shown to drive DIO and its complications as nonhematopoietic cell TF/FVIIa/PAR-2 signaling promotes obesity through the suppression of Akt phosphorylation (52). Along the same lines, mice either lacking PAR-2 or the cytoplasmic domain of TF were protected against DIO and IR (52). Moreover, the genetic ablation of TF/PAR-2 signaling in hematopoietic cells or the pharmacological inhibition of macrophage TF significantly reduced AT macrophage infiltration and inflammation (52). Collectively, these findings suggest that increased thrombin activity and PARs cleavage drive AT inflammation in states of metabolic dysfunction. Nevertheless, such mechanisms have not been assessed in the PPAT of metabolically dysfunctional animal models. More importantly, the consequences of the inhibition of PPAT thromboinflammatory processes on prostatic neoplastic alterations secondary to metabolic dysfunction have not been investigated.

## CHAPTER II

### OBJECTIVE, SPECIFIC AIMS, AND SIGNIFICANCE

Our laboratory has shown, in a prediabetic rat model, that the consumption of a mild hypercaloric (MHC) diet is associated with the emergence of localized AT inflammation that drastically affects proximal tissues (70-72). Moreover, previous studies showed that metabolic dysfunction is associated with increased AT FXa levels as well as PAR1 and PAR2 expression and activity. As these factors drive PCa development and progression, we hypothesize that enhanced PPAT thromboinflammatory processes drive PCa development in prediabetes and that the interruption of thromboinflammation through the direct inhibition of FXa reduces the burden of PPAT inflammation on the prostate.

Thus, we aimed to:

1. Investigate the impact of rivaroxaban treatment on the gross metabolic aspects and PPAT inflammation in prediabetic rats.
2. Assess the impact of rivaroxaban on the primitive prostatic neoplastic alterations evoked by prediabetes.
3. Investigate the potential molecular mechanisms of rivaroxaban by studying its impact on PCa cell survival proliferation, migration, and colony formation capacity *in vitro*.

## CHAPTER III

### MATERIALS AND METHODS

#### **A. Animal Model and Experimental Design**

All animal experiments in this study were conducted in accordance with study protocol number 16-10-386 approved by the American University of Beirut Institutional Animal Care and Use Committee (IACUC) in compliance with the Guide for the Care and Use of Laboratory Animals of the Institute for Laboratory Animal Research of the National Academy of Sciences, U.S.A. Male Sprague-Dawley rats (5-6 weeks of age; 150g) were randomly allocated to three different groups (n=8 each): (1) a control group comprising rats maintained on normal chow diet (3 Kcal/g, CTRL) for 12 weeks, (2) an experimental group comprising rats maintained on a mild hypercaloric diet (4.035 Kcal/g; MHC) for 12 weeks, and (3) an experimental group comprising rats maintained on a mild hypercaloric diet (4.035 Kcal/g; MHC) for 12 weeks during which rivaroxaban (20mg/kg mixed with chow; RIVA) treatment was initiated at week 10 and continued for the remaining 2 weeks. The dose of rivaroxaban treatment corresponds to one that is not associated with hemorrhagic reactions, as shown in our previous studies. Additionally, MHC and RIVA rats were supplemented with 20% v/v fructose water for 2 weeks starting week 10 to further instigate hyperinsulinemia and adipose tissue inflammation. Rats were maintained in an ambient temperature- and humidity-controlled environment under a 12-hour light/dark cycle. MHC diet (4.035 Kcal/g distributed as follows: 15.8% from protein, 18.06% from fat (of which 5% by weight saturated fat), and 46.13% from carbohydrates) was prepared in-house using a base of Envigo diet (3 Kcal/g distributed as follows: 32% from protein, 14% from fat (of which 0.9% by weight saturated fat), and 54% from carbohydrates) (Teklad Rodent Diets, Madison, WI), to which food grade fructose (20%

w/w, Santiveri Foods, Spain) and hydrogenated vegetable oil (15% w/w, Mazola, BFSA) were added and homogenously mixed after correction for displaced electrolytes and vitamins. Rats were individually caged and had *ad libitum* access to water and food. Weekly body weight and food intake were recorded using a digital balance and calorie intake and energy efficiency were calculated.

### **B. Random Blood Glucose Measurement and Intraperitoneal Glucose and Insulin Tolerance Tests**

Following the intended feeding duration, blood glucose level measurement was done using Accu-Check Performa glucometer (Roche Diagnostics, Rotkreuz, Switzerland). IpGTT was performed as previously described with slight modification (70). Briefly, rats were fasted for 6 hours and were then administered 2 g/Kg glucose (Thermo Fisher Scientific, Waltham, MA) intraperitoneally and blood glucose levels were recorded using the Accu-Check Performa glucometer at baseline, 15, 30, 60, and 120 minutes following the injection. For IpITT, rats were administered 1 IU/Kg insulin (Actrapid recombinant human insulin, Novo Nordisk, Denmark) following a 6 hour long fast and blood glucose levels were recorded using the Accu-Check Performa glucometer at baseline, and 15, 30, 60, 90, 120, and 180 minutes thereafter. Area under curve of the plotted recorded values were calculated.

### **C. Noninvasive Hemodynamics, Body Composition, Organ Harvest, Serum Collection, and Serum Analysis**

Following the intended feeding duration, systolic blood pressure was measured noninvasively by tail cuff using a CODA high-throughput monitor (Kent Scientific, Torrington, CT) as previously described (72). Irregular and unacceptable recordings were

noted as false recordings by the system and were excluded from further analysis. The body composition of immobilized rats was analyzed using a nuclear magnetic resonance (NMR) (LF10 Minispec NF4433, Bruker, MA, USA) and the parameters recorded were fat mass, lean mass, and fluid content (values obtained from each rat were compared to a standardized and calibrated rat). The fat/lean ratio was calculated to detect differential tissue density.

On sacrifice, rats were anesthetized by 50 mg/mL thiopental and organs and blood were collected following decapitation. Ventral prostate and periprostatic adipose tissue were weighed and then either placed in formaldehyde for further histological analysis or snap-frozen in liquid nitrogen and stored at -80°C for molecular studies. Correlations between periprostatic adipose tissue mass and that of the ventral prostate or rat body weight were calculated. Blood samples (6-8 mL) were centrifuged at 5,000 rpm for 10 minutes and serum was isolated and stored at -80°C until the time of analysis. Serum triglycerides were quantified using a Fluitest assay kit (Biocon Diagnostik, Möchberg, Germany) according to the manufacturer's instructions. Rat serum levels of insulin were measured using an ELISA kit according to the manufacturer's protocol (Invitrogen, Thermo Fisher Scientific, Waltham, MA, USA).

#### **D. Histopathology, Immunohistochemistry, and Immunofluorescence**

Prostate and PPAT sections (4 µm) of paraffin-embedded tissues were stained with Hematoxylin & Eosin (H&E) for histological assessment. Adipocyte expansion, adipocyte size distribution, and the number of adipocytes per image area were assessed using the plugin Adiposoft on ImageJ (Fiji) (73). The formation of prostatic intraepithelial neoplasia (PIN), acinus luminal area, and epithelial thickness were assessed in prostate

sections. Masson's trichrome staining was used to assess tissue fibrosis and toluidine blue staining was used to assess tissue mast cell infiltration. Trichrome and toluidine blue stainings were semi-automatically quantified in representative field images captured using an Olympus CX41 light microscope (Olympus, Tokyo, Japan) and expressed as a percentage of staining of total surface area, and the results from all fields were averaged.

Fibrin deposition in PPAT sections was assessed using a modified version of Carstairs's method as previously described (74). Briefly, paraffin-embedded sections were deparaffinized and placed in Ferric Alum for 5 minutes. Section slides were then washed in running tap water and stained with Mayer's hematoxylin for 5 minutes. Following washing with running tap water, slides were placed in picric acid-orange G solution for 1 hour. Slides were then rinsed and placed in Ponceau-fuchsin solution for 5 minutes. Slides were then rinsed in distilled water and treated with 1% phosphotungstic acid solution for 5 minutes followed by rinsing in distilled water and staining with aniline blue solution for 30 minutes. Finally, slides were rinsed in several changes of distilled water to remove residual stainings, dehydrated, and mounted. Carstairs's method produces differential staining of fibrin (bright red), platelets (gray-blue to navy), collagen (bright blue), muscle (red), and red blood cells (yellow). Carstairs's fibrin staining was semi-automatically quantified in representative field images captured using an Olympus CX41 light microscope (Olympus, Tokyo, Japan) and expressed as a percentage of staining of total surface area, and the results from all fields were averaged. All solutions were filtered through 0.2 $\mu$ m filters prior to use.

Immunohistochemical detection of PPAT CD68, tyrosine hydroxylase (TH), VEGF-A, and Beta-3 adrenergic receptor ( $\beta_3$ -AR) was performed using 1:1000 concentrations of rabbit anti-CD68 (ab53444, Abcam, Cambridge, UK), rabbit anti-TH



(2792S, Cell Signaling, Danvers, MA), rabbit anti-VEGF-A (MBS2544687, MyBioSource, San Diego, California, USA), and rabbit anti- $\beta_3$ -AR (MBS8220053, MyBioSource, San Diego, California, USA). The detection of prostate CD68, the nuclear protein ki67, proliferating cell nuclear antigen (PCNA), Slug, and Snail was performed using 1:1000 concentrations of rabbit anti-CD68, rabbit anti-ki67 (ab15580, Abcam, Cambridge, UK), rabbit anti-PCNA (ab152112, Abcam, Cambridge, UK), mouse anti-Slug (#9589, Cell Signaling, Danvers, MA), and rabbit anti-Snail (#3879, Cell Signaling, Danvers, MA). Signal was visualized using the Novolink Polymer Detection Kit (Leica Biosystems, Buffalo Grove, IL) according to the manufacturer's protocol following antigen retrieval (citrate antigen retrieval buffer (pH=6) for 1 hour in a steamer) and overnight incubation with the respective antibodies at 4°C in a humidified chamber. Control experiments were performed by omitting primary antibodies and using rabbit IgG (immunoglobulin G) controls. Images were taken using the Olympus CX41 light microscope. As for periprostatic adipose tissue CD68 staining, the number of crown-like structures, which correspond to apoptotic adipocytes surrounded by at least three distinct macrophages, per image area was evaluated.

Periprostatic adipose tissue and prostate ROS load was detected using dihydroethidium (DHE) staining as previously described (71). Fluorescent images of ethidium-stained sections were acquired using a Zeiss LSM 710 laser scanning confocal microscope (Zeiss, Oberkochen, Germany) and were detected through the Alexa Fluor 568 (AF568) filter for the DHE red fluorescent labeling indicating superoxide production. Random areas were acquired per section and the average pixel intensity corresponding to each animal was compared among groups. Zen light software (2.3 blue version) was used

for signal intensity thresholding and quantification and values were expressed as fluorescence intensity (arbitrary units).

Indirect immunofluorescence analysis was used to assess prostate epithelial basal to luminal migration and epithelial to mesenchymal transition. Briefly, paraffin-embedded tissues were deparaffinized and subjected to antigen retrieval following which sections were allowed to cool to room temperature. Sections were then washed and incubated with protein blocking buffer (10% normal goat serum (NGS), 0.1% Triton X-100, 3% bovine serum albumin (BSA) in PBS) for 1 hour to block non-specific binding. Sections were then washed twice with PBST (0.05% Tween-20 in PBS) and incubated with 1:200 rabbit anti-cytokeratin 5 (CK5) (PRB-160P, BioLegend, Dedham, MA, USA), 1:200 mouse anti-CK8 (Clone 1E8, BioLegend, Dedham, MA, USA), 1:200 rabbit anti-alpha smooth muscle actin ( $\alpha$ -SMA) (ab5694, abcam, Cambridge, UK), or 1:200 anti-vimentin (sc-7557Fs, Santa Cruz Biotechnology, Santa Cruz, California, USA) in primary antibody diluent solution (2% NGS, 0.1% Triton X-100, and 3% BSA in PBS) overnight at 4°C in a humidified chamber. Slides were then washed twice with PBST and were incubated with secondary 1:200 goat anti-mouse AF568 (A-11004, Invitrogen, Thermo Fisher Scientific, Waltham, MA, USA) and 1:200 goat anti-rabbit AF488 (A-11008, Invitrogen, Thermo Fisher Scientific, Waltham, MA, USA) antibodies in secondary antibody diluent (2% NGS and 0.1% Triton X-100 in PBS) at 37°C for two hours in the dark. Finally, slides were rinsed three times in PBST and were mounted using Fluoroshield Mounting Medium with 4',6-diamidino-2-phenylindole (DAPI) (ab104139, abcam, Cambridge, UK). Following the same protocol, PPAT sections were stained with 1:1000 concentrations of rabbit anti-CD31 (sc-1506R, Santa Cruz Biotechnology, Santa Cruz, California, USA) followed by 1:200 goat anti-rabbit AF488 (A-11008, Invitrogen,

Thermo Fisher Scientific, Waltham, MA, USA) and 1:1000 Phalloidin-TRITC (CS207796, Millipore, Temecula, California) to simultaneously visualize blood vessel endothelial linings and adipocyte cytoskeletal structures. Random tile scans were acquired using the laser-scanning confocal microscope for quantification, while representative images were presented through Z-stacked images. Zen light software was used for thresholding and quantification of fluorescent intensity and values were expressed as fluorescent intensity (arbitrary units).

#### **E. Determination of Macrophage Polarization by Fluorescence-Activated Cell Sorting**

Stromal vascular cells were isolated from freshly dissected PPAT and ventral prostate as previously described with slight modifications (72). Proinflammatory M1-polarized macrophages were identified based on the simultaneous expression of the surface markers CD45, CD68, and CD86. Briefly, freshly dissected tissues were weighed and finely minced in serum-free Dulbecco's modified eagle medium - nutrient mixture F12 Ham (DMEM-F12 Ham) (Sigma Aldrich, St. Louis, MO, USA) on ice. Minced tissues were incubated in tissue digestion buffer (0.5% BSA in DMEM-F12 Ham) containing 5 mg/mL Collagenase II (17101-015, Gibco, Life Technologies Corporation, Grand Island, NY, USA) (1 mg/mL for PPAT) at 37°C for 90 minutes with continuous rotation. Prostate was further digested in trypsin (Sigma Aldrich, St. Louis, MO, USA) for 15 minutes at 37°C with continuous rotation. Cell slurry was then filtered through a prewetted 40 µm cell strainer and gently washed with fluorescence-activated cell sorting (FACS) buffer containing 1% fetal bovine serum (FBS) (Sigma Aldrich, St. Louis, MO, USA). Cell slurry was then centrifuged at 500g for 10 minutes at 4°C and the pellet containing stromovascular cells was resuspended and incubated in RBC lysis buffer for

5 minutes. RBC lysis buffer was then neutralized by FACS buffer, cell slurry centrifuged, and the pellet resuspended in FACS buffer. An aliquot of the stromal fraction containing  $10^6$  cells was incubated in FACS buffer containing 1:100 DAPI, 1:50 APC-Cy780-conjugated anti-CD45, 1:10 phycoerythrin (PE)-conjugated anti-CD68, and 1:125 fluorescein isothiocyanate (FITC)-conjugated anti-CD86 (Thermo Fisher Scientific, Waltham, MA) on ice for 30 minutes in the dark. Cells were gently washed twice and resuspended in FACS buffer. Stained cells were counted using a BD FACSAria Cell Sorter (BD Biosciences, San Jose, CA), and the abundance of M1 macrophages as a percentage of all macrophages was evaluated. Antibody-beads mixtures and unstained cells were used to set compensation and gating. All buffers were filtered through  $0.2\mu\text{m}$  filters prior to use.

## **F. Cell Culture**

Murine *Pten*<sup>-/-</sup> *p53*<sup>-/-</sup> Plum-AD prostatic epithelial cells were previously generated from androgen-dependent orthotopic tumors (PIN/ adenocarcinoma) (75). Cells were cultured in advanced DMEM-F12 (12634-010, Gibco, Life Technologies Corporation, Grand Island, NY, USA) supplemented with 2% FBS (Sigma Aldrich, St. Louis, MO, USA), 1% Penicillin-Streptomycin mixture (L0022-100, Biowest, MO, USA), 1% Glutamax TM-I (100X) (35050-061, Gibco, Life Technologies Corporation, Grand Island, NY, USA), 1% HEPES Buffer Solution 1M (15630-056, Gibco, Life Technologies Corporation, Grand Island, NY, USA), 0.2% Gentamicin/Amphotericin B 500X (50-0640, Gibco, Life Technologies Corporation, Grand Island, NY, USA), 0.2% Plasmocin Prophylactic (ant-mpp, InvivoGen, San Diego, CA, USA), and 0.001% recombinant human epidermal growth factor (EGF) (PHG0311, Gibco, Life

Technologies Corporation, Grand Island, NY, USA) at 37°C in a humidified 5% CO<sub>2</sub> incubator. Cells were propagated using regular trypsinization techniques after becoming 80% confluent. Occasional bright field phase contrast images were taken using an inverted light microscope to evaluate cellular morphological changes.

Pharmaceutical grade Rivaroxaban was a kind gift from regional manufacturers (Pharo Pharma and Hikma Pharmaceuticals) and was dissolved in dimethyl sulfoxide (DMSO). PAR-2 (1-6) amide (mouse, rat) trifluoroacetate salt (S9317, Sigma Aldrich, St. Louis, MO, USA) was dissolved in sterile deionized water. All solutions were filtered through 0.2µm filters prior to use.

### **G. Cell Proliferation, Cell Growth Inhibition, and Cell Viability Assays**

Cell proliferation was determined by MTT ([3-(4,5-dimethylthiazol-2-yl)-2,5-diphenyltetrazolium bromide]) (M5655, Sigma Aldrich, St. Louis, MO, USA) assay as previously described, which entails MTT reduction by NAD-dependent dehydrogenase activity (76). Briefly, 3,000 cells were seeded in 96 well plates and allowed to adhere for 24 hours. Cells were thereafter treated with increasing concentrations of rivaroxaban and PAR-2 and their combination for 24 hours. MTT (5 mg/mL in DMSO) was added to each well and incubated at 37°C for 3 hours, after which MTT stop solution (0.2% 6M HCl, 5% isobutanol, and 10% SDS in deionized water) was used to dissolve violet formazan crystals. Plates were incubated at 37°C overnight to ensure sufficient crystal solubilization. Thereafter, MTT optical density (OD) was measured at the wavelength 595 nm using an ELISA microplate reader (Multiskan Ex, Thermo Fisher Scientific, Waltham, MA, USA). Metabolic activity was expressed as a percentage of control cells

and following the normalization to their relative vehicles. The experiments were carried out in quadruplicates.

Cell growth inhibition was assessed using the Sulforhodamine B (SRB) assay. Briefly, 3,000 cells were seeded in 96 well plates and allowed to adhere for 24 hours. Cells were thereafter treated with increasing concentrations of rivaroxaban and PAR-2 and their combination for 24 hours. Cells were then fixed using trichloroacetic acid (TCA) solution for one hour at 4 °C, washed four times with deionized water, and allowed to dry at room temperature overnight. Then, 50 µL of 0.04% SRB (S1402, Sigma Aldrich, St. Louis, MO, USA) solution was added to each well followed by four washes with 1% acetic acid and wells were allowed to dry. Finally, 100 µL of Tris base solution (PH 10.5) was added to allow for the dissociation of the stoichiometrically bounded proteins and the optical density was determined using a microplate spectrophotometer set at 492 nm. Experiments were carried out in quadruplicates and values were expressed relative to respective vehicles.

Propidium iodide (PI) exclusion assay was used to assess cell viability. Plum-AD cells were seeded at a density of 50,000 cells per well in 12-well plates. Following respective treatments, cells were washed with PBS, trypsinized, collected and pelleted. Cells were resuspended in 5µg/mL PI (81845, Sigma Aldrich, St. Louis, MO, USA) in PBS for ten minutes and the percentage of PI-positive cells were recorded using a Guava EasyCyte8 Flow Cytometer. Unstained and positive controls were run simultaneously to allow for proper cell gating. Experiments were carried out in quadruplicates and the acquired data was analyzed using the FlowJo software.

## **H. Cell Cycle Analysis**

Plum-AD cells were seeded at a density of 50,000 cells per well in 12-well plates. Following respective treatments, cells were washed with ice-cold PBS, collected, and fixed with ice-cold 70% ethanol for 30 minutes. Cells were then incubated at 37 °C for 30 minutes in PBS solution containing 10 µg/mL RNase (10109134001, Roche Diagnostics, Rotkreuz, Switzerland) and 5 µg/mL PI. The percentages of cells belonging to distinct cell cycle phases were determined using a Guava EasyCyte8 Flow Cytometer. Experiments were carried out in quadruplicates and the acquired data was analyzed using the GuavaSoft™ 2.7 Software.

## **I. Assessment of Cellular Oxidative Stress**

The formation of ROS was evaluated in Plum-AD cells using the fluorogenic probe DHE. Plum-AD cells were seeded at a density of 50,000 cells per well on glass coverslips in 12-well plates and were allowed to adhere for 24 hours. Cells were treated with 100 µM rivaroxaban (predetermined as the highest concentration not showing significant reduction of cell viability) for 24 hours. Cells were then fixed in 4% paraformaldehyde (PFA) and then permeabilized. Cells were then incubated in 5nM DHE working solution (D23107, Invitrogen, Thermo Fisher Scientific, Waltham, MA, USA) for 1 hour at 37°C, which was then followed by three washes with PBS. Coverslips were then mounted using Fluoroshield Mounting Medium with DAPI (ab104139, abcam, Cambridge, UK), and were imaged using a Zeiss LSM 710 laser scanning confocal microscope (Zeiss, Oberkochen, Germany). DHE signal observed through the AF568 filter was normalized to the number of DAPI-positive nuclei per image and the values

corresponding to each condition were averaged. Experiments were done in quadruplicates.

Nitroblue tetrazolium (NBT) reduction assay was used to assess cellular ROS content. This assay entails the formation of blue-black formazan compound following NBT reduction by free oxygen radicals (77). Plum-AD cells were seeded at a density of 10,000 cells per well in 96-well plates and were allowed to adhere for 24 hours. Cells were treated with 10  $\mu$ M rivaroxaban for 24 hours followed by the addition of 100  $\mu$ L of a 1mg/mL NBT working solution (298-83-9, Sigma Aldrich, St. Louis, MO, USA) and incubation for 1 hour at 37°C. Wells were washed with 100% methanol for 10 minutes and wells were allowed to air-dry. 120  $\mu$ L of 2M potassium hydroxide (KOH) solution and 140  $\mu$ L of DMSO were then added to each well and absorbance was determined at 630 nm using an ELISA microplate reader (Multiskan Ex, Thermo Fisher Scientific, Waltham, MA, USA). The experiment was carried out in quadruplicates and the relative ROS production was calculated.

#### **J. Assessment of Mitochondrial Membrane Potential**

The fluorescent mitochondrial stain Mitotracker Orange was used to assess mitochondrial membrane potential. Briefly, Plum-AD cells were seeded on coverslips at a density of 50,000 cells per well in 12-well plates and were allowed to adhere overnight. Cells were then washed with PBS once and were incubated in working solution of 200nM Mitotracker Orange CMTMRos (M7510, Invitrogen, Thermo Fisher Scientific, Waltham, MA, USA) for 30 minutes in the dark. Thereafter, coverslips were mounted using Fluoroshield Mounting Medium with DAPI (ab104139, abcam, Cambridge, UK) and images were acquired through a Zeiss LSM 710 laser scanning confocal microscope using



the AF568 filter. Mitotracker Orange stain was expressed as intensity per image area and quantified using Fiji. Experiments were run in quadruplicates.

### **K. Cell Migration Assay**

Plum-AD cells were seeded at a density of 50,000 cells per well in 12-well plates. Following the formation of a cellular monolayer, cells were washed once with PBS and incubated for 20 minutes with mitomycin (M0503, Sigma Aldrich, St. Louis, MO, USA) at a concentration of 2 $\mu$ g/mL. Cells were then washed with PBS and a scratch was made using a yellow micropipette tip. Cells were then incubated in their respective treatment conditions and images of the scratches were acquired at t=0 hours and every three hours thereafter until the closure of the untreated condition. Scratch area at each time point was quantified using Fiji and normalized to that at t=0 hours. Wound area was presented as fold change from t=0 hours.

### **L. Colony Formation Assay**

Plum-AD cells were seeded at a density of 50,000 cells per well in 12-well plates and were allowed to adhere overnight. Following respective treatments for 24 hours, cells were washed with PBS, trypsinized, and counted. 4,000 cells from each condition were then seeded in 6-well plates for 4 days. Cells were then washed with PBS, fixed with 95% ethanol, and stained with 0.2% crystal violet for 5 minutes. Viable cellular colonies were counted and were expressed relative to those of the vehicle treated condition. Experiments were run 6 times and values are expressed as mean  $\pm$  S.E.M.

### **M. Statistical Analysis**

Data were expressed by Mean  $\pm$  S.E.M. All analysis was done using GraphPad Prism software. Comparisons between different experimental groups were done using One-way ANOVA followed by Tukey's post-hoc test and Two-way ANOVA followed by Sidak's multiple comparisons test. A P-value < 0.05 was considered statistically significant.

## CHAPTER IV

### RESULTS

#### **A. Metabolic Consequences of Mild Hypercaloric Diet Consumption**

We established three experimental groups comprising 6 rats each and consisting of regular diet-fed (CTRL), mild hypercaloric diet-fed (MHC) and MHC-fed rivaroxaban-treated (MHC+RIVA) rats (Fig. 1A). During the experimental period, MHC-fed rats, with or without rivaroxaban treatment, significantly consumed a higher cumulative caloric intake compared to control rats (Fig. 1B). Despite the significant difference in caloric consumption, MHC-fed rats, irrespective of rivaroxaban treatment, gained the same body weight (Fig. 1C). As such, MHC-fed rats exhibited reduced metabolic efficiency that was not corrected by rivaroxaban treatment (Fig. 1D). Moreover, MHC-fed rats, irrespective of rivaroxaban treatment, displayed increased fat:lean ratio that was not secondary to reduced lean mass (Fig. 1E). MHC consumption did not disturb glucose homeostasis as it was neither associated with increased random blood glucose levels nor with impaired glucose tolerance compared to control rats (Fig. 1F, 1J, and 1L). However, MHC-fed rats exhibited insulin resistance evidenced by an increased intra-peritoneal insulin tolerance test (ipITT) area under curve (AUC) compared to control rats, which was reduced back to the control levels following rivaroxaban treatment (Fig. 1K and 1M). Consistently, MHC-fed rats exhibit increased levels of circulating insulin levels compared to control rats, while rivaroxaban treatment reduced serum insulin levels back to control levels (Fig 1I). Moreover, MHC-fed rats exhibited an impaired serum lipid profile demonstrated by an increased level of serum triglycerides (Fig. 1H). Although MHC-fed rats exhibit enhanced adiposity, there exists no correlation between PPAT mass and rat weight (Fig. 1N). However, MHC-fed rats

showed increased PPAT/Ventral prostate (VP) mass compared to control mass, while rivaroxaban treatment significantly reduced PPAT/VP mass ratio (Fig. 1O).

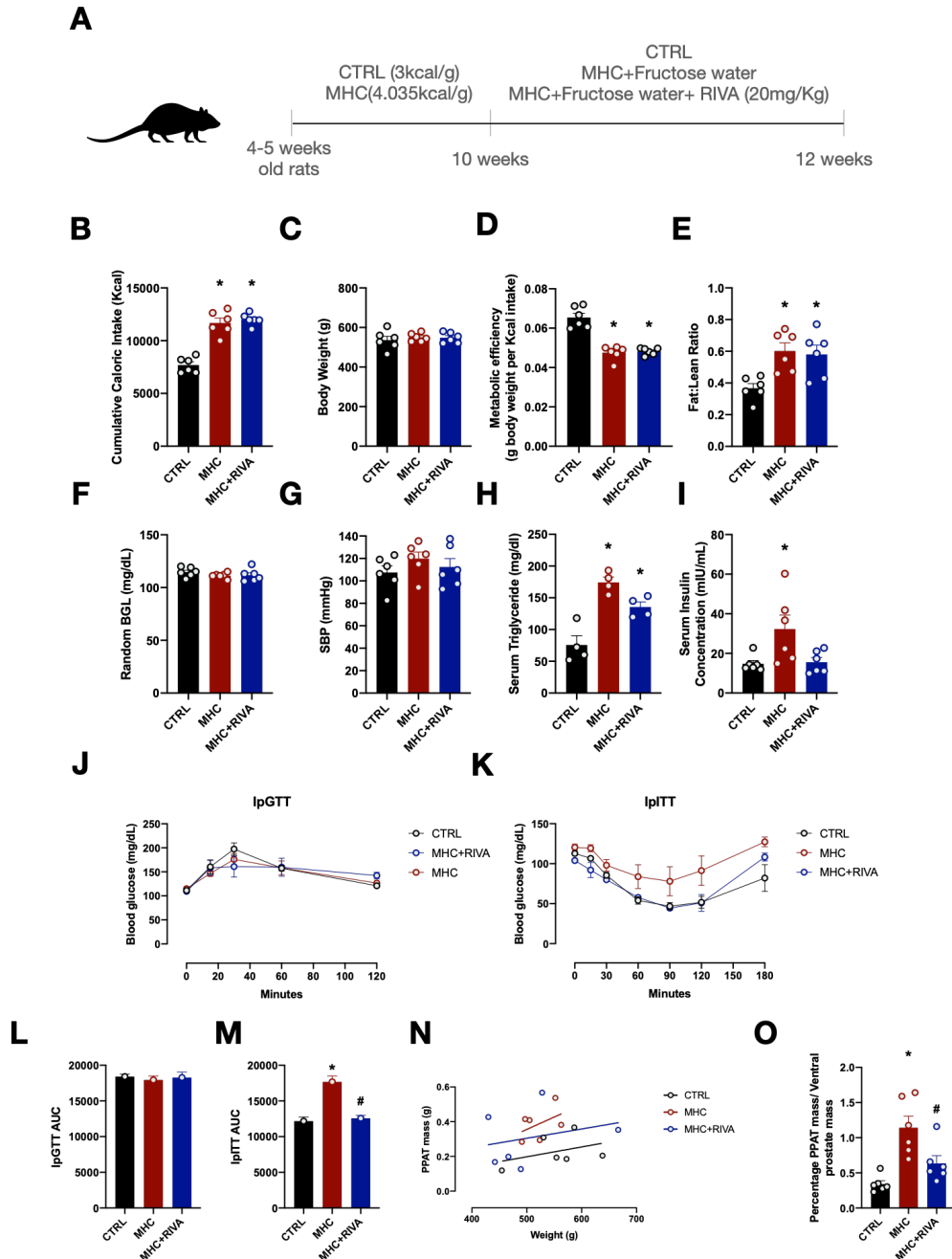


**Figure 1. Metabolic consequences of Mild Hypercaloric Diet Consumption.**

A, Schematic diagram of the experimental groups included in the study. B, Cumulative caloric intake in control versus MHC-fed and rivaroxaban-treated MHC-fed rats along the duration of 12 weeks of feeding (n=6). C, Body weight after 12-weeks of feeding for the three experimental groups (n=6). D, Metabolic efficiency calculated as the gain of body weight as a function of caloric intake (n=6). E, Body composition measured via NMR represented as fat:lean ratio for rats across the three experimental groups (n=6). F,

Random blood glucose measured using a glucometer for rats across the three experimental groups of rats (n=6). G, Non-invasive systolic blood pressure measurement across the experimental groups (n=6). H, Serum triglyceride concentrations measured across the experimental groups (n=4). I, Serum insulin concentrations measured across the experimental groups using ELISA (n=6). J-M, Intra-peritoneal glucose and insulin tolerance tests and their respective area under curves (n=4). N, PPAT mass-body weight correlation across the three experimental groups (n=6). O, Percentage of PPAT mass/ Ventral prostate mass across the experimental groups of rats (n=6). Values are Mean  $\pm$  S.E.M. Statistical significance was tested using one-way ANOVA followed by Tukey's multiple comparisons (p-value<0.05). \* denotes significance when comparing to the CTRL group while # denotes significance when comparing the MHC group.

## B. Periprostatic Adipose Tissue Dysfunction is a Hallmark of Prediabetes

The increased PPAT mass to VP mass ratio prompted us to investigate PPAT adipocyte expansion and the ensuing tissue dysfunction and inflammation. PPAT adipocytes undergo significant diametric expansion in MHC-fed rats compared to control rats, while rivaroxaban treatment was associated with reduced adipocyte size (Fig. 2A-D).

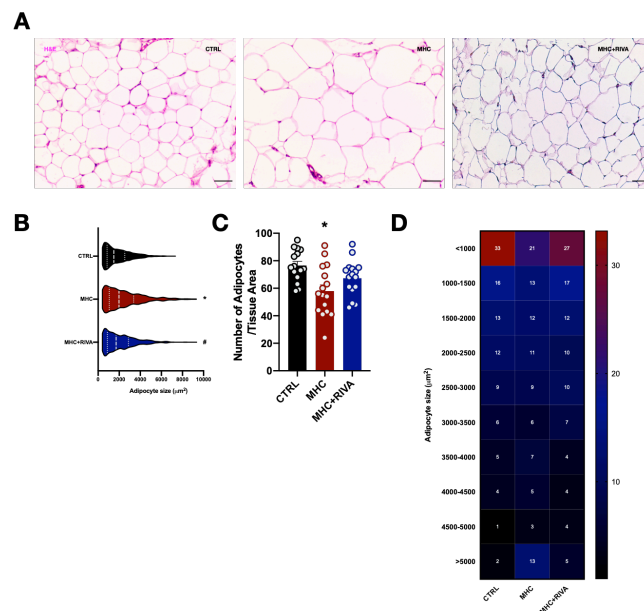


**Figure 2. Periprostatic adipose tissue expansion is a hallmark of prediabetes.**

A, Representative hematoxylin and eosin staining of PPAT from the three experimental rat groups. B-D, PPAT adipocyte size analysis, number of cells per tissue area, and adipocyte size distribution (n=4). Values are Mean  $\pm$  S.E.M. Statistical significance was tested using one-way ANOVA followed by Tukey's multiple comparisons (p-

value<0.05). \* denotes significance when comparing to the CTRL group while # denotes significance when comparing the MHC group.

No significant fibrosis was detected across the three experimental groups evidenced by unaltered Masson Trichrome staining intensity (Fig. 4A and 4B). MHC-fed rats exhibited PPAT with enhanced ROS evidenced by increased DHE staining, that was decreased with rivaroxaban treatment (Fig. 3A and 3B).

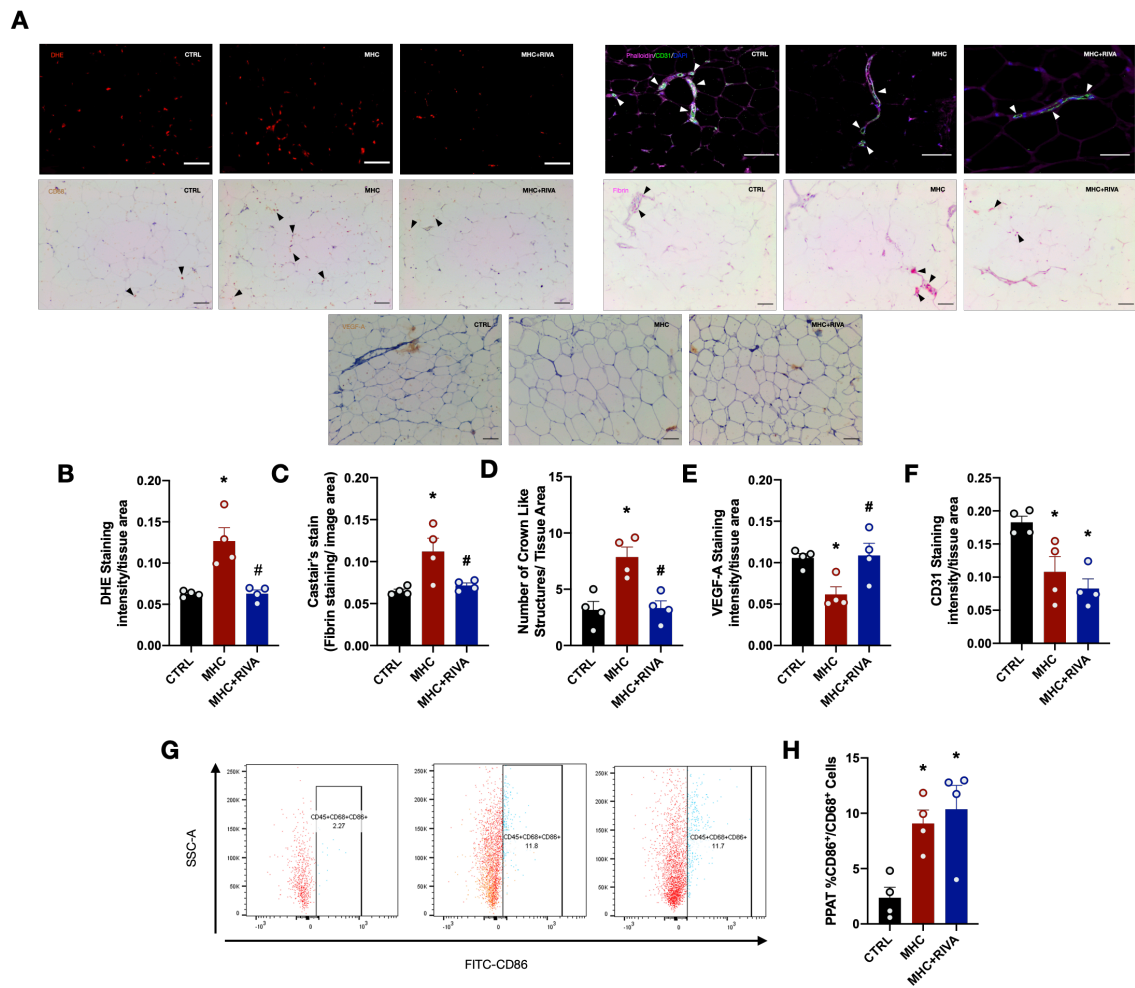


### Figure 3. Rivaroxaban modulates metabolic dysfunction-driven periprostatic adipose tissue thromboinflammation.

**A**, Representative images depicting PPAT DHE, CD31, CD68, VEGF-A and Carstairs' staining. **B-F**, Quantification of PPAT DHE, CD31, CD68, VEGF-A and Carstairs' staining (n=4). **G**, Representative scatter plots depicting PPAT abundance of CD45<sup>+</sup>CD68<sup>+</sup>CD86<sup>-</sup> and CD45<sup>+</sup>CD68<sup>+</sup>CD86<sup>+</sup> macrophages. **H**, Quantification of PPAT-infiltrating proinflammatory macrophages as a percentage of total macrophages in PPAT stromovascular cells (n=4). Values are Mean ± S.E.M. Statistical significance was tested using one-way ANOVA followed by Tukey's multiple comparisons (p-

value<0.05). \* denotes significance when comparing to the CTRL group while # denotes significance when comparing the MHC group.

We detected tyrosine hydroxylase (TH)-expressing PPAT-innervating sympathetic neurons and Beta3 adrenergic receptor ( $\beta_3$ -AR)-expressing adipocytes (Fig. 4A, 4D, and 4E). However, we detected no alteration in the expression of TH and  $\beta_3$ -ARs across the three experimental groups. Although PPAT expression of VEGF-A is significantly reduced in MHC-fed rats, vascular density evidenced by CD31 positive staining is also reduced (Fig. 3A, 3E, and 3F). Rivaroxaban treatment is associated with increased PPAT VEGF-A expression albeit no change of vascular density in compared to MHC-fed rats. These pathological morphological and molecular alterations observed in the PPAT of MHC-fed rats is associated with enhanced extravascular fibrin deposition (Fig. 3A and 3C).

Consistent with PPAT dysfunction, we detected increased PPAT macrophage infiltration evidenced by increased CD68-positive staining but no significant change in PPAT mast cell abundance (Fig. 3A and 3D and Fig. 4A and 4C). Indeed, CLS formation was significantly increased in the PPAT of MHC-fed rats compared to control rats, while rivaroxaban appears to limit PPAT macrophage infiltration. Furthermore, we isolated PPAT stromovascular cells and profiled PPAT-infiltrating macrophages using FACS. The percentage of proinflammatory CD45<sup>+</sup>CD68<sup>+</sup>CD86<sup>+</sup> macrophages significantly increased in MHC-fed rats and rivaroxaban-treated MHC-fed rats to similar extents in comparison to control rats (Fig. 3G and 3H).

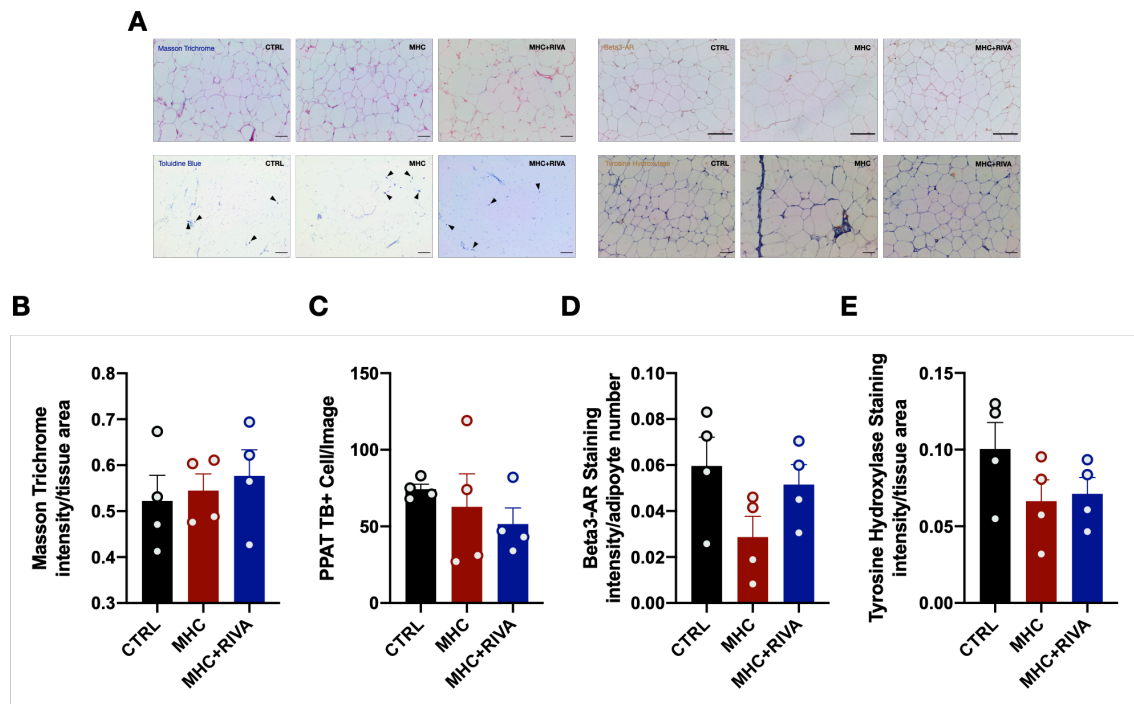


**Figure 4. Periprostatic adipose tissue exhibits no pro-fibrotic or pro-thermogenic phenotype in prediabetes.**

**A**, Representative images depicting PPAT Masson trichrome, toluidine blue, Beta-3 adrenergic receptor and tyrosine hydroxylase staining. **B-E**, Quantification of PPAT Masson trichrome, toluidine blue, Beta-3 adrenergic receptor and tyrosine hydroxylase staining (n=4). Values are Mean  $\pm$  S.E.M. Statistical significance was tested using one-way ANOVA followed by Tukey's multiple comparisons (p-value<0.05).

### **C. Periprostatic Adipose Tissue Dysfunction is Associated with Early Prostatic Neoplastic Alterations in Prediabetes**

Morphological assessment of the prostates demonstrated that MHC-fed rats exhibited prostates with increased epithelial thickness and enhanced formation of prostatic intraepithelial neoplasia (PIN) compared to the prostates of control rats, albeit no significant change in acinar luminal area was detected (Fig5. A-D). Remarkably, rivaroxaban treatment in MHC-fed rats reduced epithelial thickness and PIN formation. Moreover, MHC-fed rats showed prostates with enhanced expression of the epithelial luminal marker CK8, indicating increased epithelial thickness (Fig6. A and Fig6. E). Importantly, we detected marked basal-to-luminal epithelial migration into acinar lumens



in MHC-fed rats evidenced by the occurrence of intraluminal CK8-expressing cells (Fig6. A).

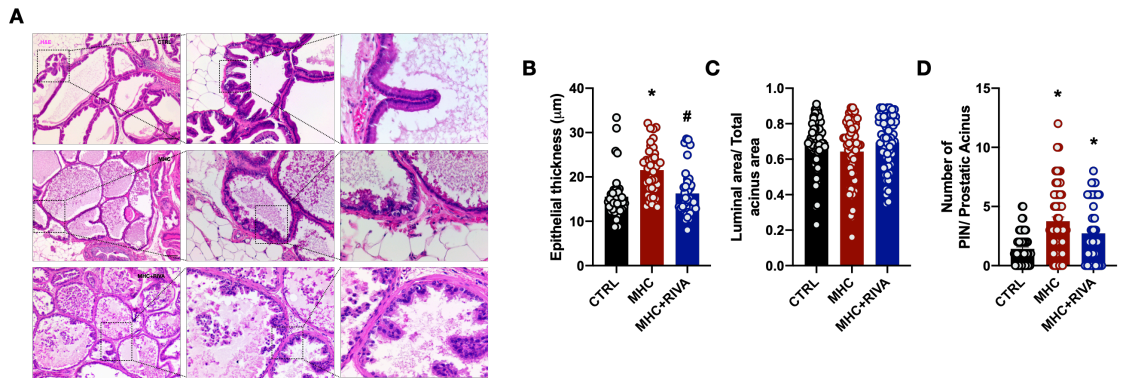


**Figure 5. Rivaroxaban modulates early prostatic neoplastic alterations secondary to mild metabolic dysfunction.**

**A**, Representative hematoxylin and eosin staining of the prostate from the three experimental rat groups. **B-D**, Quantification of epithelial thickness (40 acini/ group), luminal area (60 acini/ group), and prostatic intraepithelial neoplasia (60 acini / group). Values are Mean  $\pm$  S.E.M. Statistical significance was tested using one-way ANOVA followed by Tukey's multiple comparisons ( $p$ -value $<0.05$ ). \* denotes significance when comparing to the CTRL group while # denotes significance when comparing the MHC group.

MHC-fed rat prostates exhibited enhanced Masson Trichome's, DHE, and toluidine blue stainings compared to those of control rats indicating enhanced fibrosis, ROS generation, and mast cell infiltration (Fig6. A-D). Rivaroxaban treatment in MHC-fed rats reduced DHE and Masson Trichome's staining intensities suggesting the resolution of MHC-induced prostatic fibrosis and oxidative stress. In addition to enhanced mast cell infiltration, prostates from MHC-fed rats exhibited increased CD68 staining indicating pronounced macrophage infiltration compared to those of control rats, while rivaroxaban treatment seemed to inhibit prostatic macrophage infiltration (Fig6. A and Fig6. F). Furthermore, we profiled prostate-infiltrating macrophages polarization following the isolation of prostatic stromovascular cells. We demonstrate that the percentage of CD45<sup>+</sup>CD68<sup>+</sup>CD86<sup>+</sup> macrophages significantly increased in MHC-fed rats

and rivaroxaban-treated MHC-fed rats to similar extents in comparison to control rats (Fig6. G and Fig6. H).

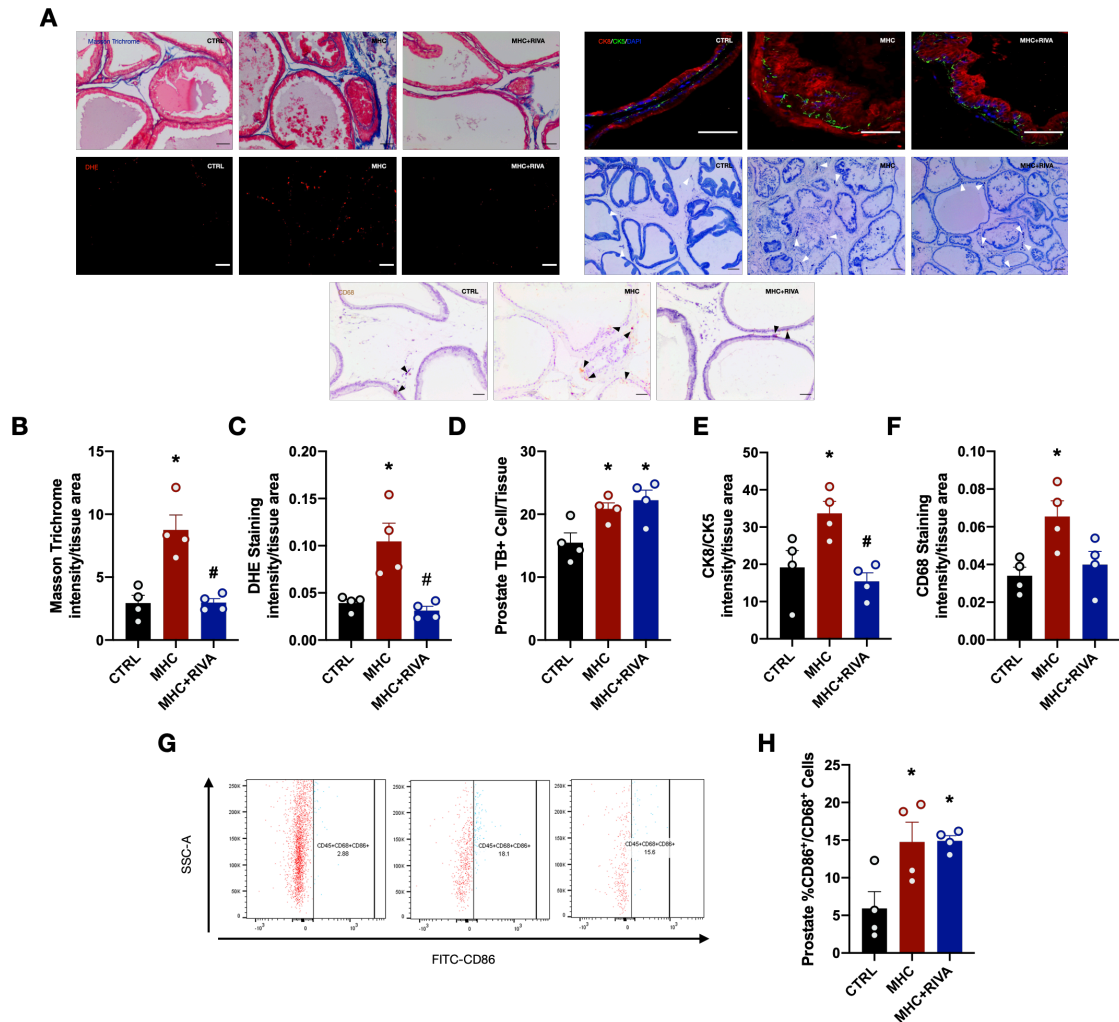


**Figure 6. Rivaroxaban modulates prostatic tissue remodeling and inflammation secondary to metabolic dysfunction.**

**A**, Representative images depicting prostate Masson trichrome, DHE, cytokeratin8/ Cytokeratin5, toluidine blue and CD68 staining. **B-F**, Quantification of prostate Masson trichrome, DHE, cytokeratin8/ Cytokeratin5, toluidine blue and CD68 staining (n=4). **G**, Representative scatter plots depicting ventral prostate abundance of CD45<sup>+</sup>CD68<sup>+</sup>CD86<sup>-</sup> and CD45<sup>+</sup>CD68<sup>+</sup>CD86<sup>+</sup> macrophages. **H**, Quantification of prostate-infiltrating proinflammatory macrophages as a percentage of total macrophages in the prostate stromovascular cells (n=4). Values are Mean ± S.E.M. Statistical significance was tested using one-way ANOVA followed by Tukey's multiple comparisons (p-value<0.05). \* denotes significance when comparing to the CTRL group while # denotes significance when comparing the MHC group.

Consistent with the increased prostatic epithelial thickness, we detected enhanced expression of the proliferation markers Ki67 and PCNA in the prostates of MHC-fed rats compared to those of the control rats indicating hyperproliferation (Fig7. A-C). Rivaroxaban treatment was associated with reduced expression of ki67 and PCNA indicating a possible anti-proliferative activity of rivaroxaban on prostatic epithelial cells *in vivo*. We also detected pronounced increase in the expression of the transcription factors Snail and Slug and the cytoskeletal protein vimentin but not of  $\alpha$ -SMA (Fig7. A and Fig7. D-G), indicative of epithelial to mesenchymal transition (EMT), a hallmark of cancer initiation (78).

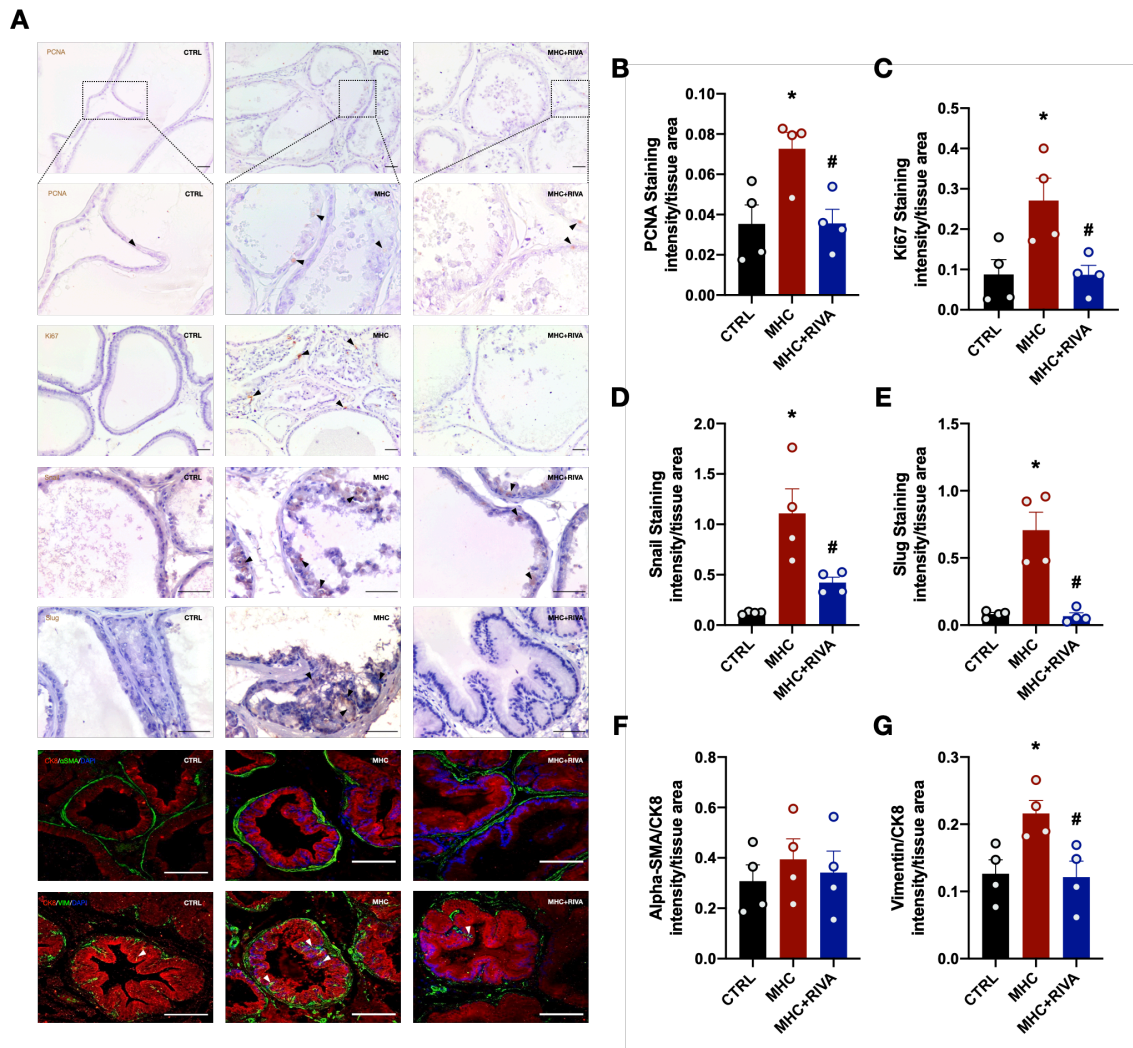


**Figure 7. Rivaroxaban ameliorates metabolic impairment-associated prostatic epithelial hyperproliferation and epithelial-to-mesenchymal transition.**

**A**, Representative images depicting prostate Ki67, PCNA, Snail, Slug, vimentin,  $\alpha$ -SMA, and CK8 immunostaining. **B-G**, Quantification of prostate Ki67, PCNA, Snail, Slug, vimentin,  $\alpha$ -SMA, and CK8 immunostaining (n=4). Values are Mean  $\pm$  S.E.M. Statistical significance was tested using one-way ANOVA followed by Tukey's multiple comparisons (p-value<0.05). \* denotes significance when comparing to the CTRL group while # denotes significance when comparing the MHC group.

#### **D. Protease-activated Receptor 2 Agonism Modulates Rivaroxaban Effects on Prostate Cancer Cells *in vitro***

As rivaroxaban was shown to halt the augmentation of prostatic epithelial thickness *in vivo*, we thought out to investigate its antiproliferative activity *in vitro*. To that end, we utilized PIN-derived, murine *Pten*<sup>-/-</sup> *p53*<sup>-/-</sup> cells. Rivaroxaban was shown to exhibit significant cytotoxicity at concentrations ranging between 100 and 1000  $\mu$ M

evidenced by a reduction of cellular metabolic activity, cellular viability, and compromised cellular membrane integrity (Fig8. A, B, and C). Subsequent experiments were carried out using a 100  $\mu\text{M}$  concentration of rivaroxaban as the least cytotoxic, non-lethal concentration. PAR-2 exhibited no cytotoxicity at concentrations ranging between 1 and 100  $\mu\text{M}$  (Fig8. A). As 5  $\mu\text{M}$  PAR-2 was shown to induce downstream signaling of PAR-2 *in vitro*, this concentration was used for subsequent experiments. While PAR-2 agonism by itself did not significantly alter cellular viability, PAR-2 agonism reversed rivaroxaban-induced reduction in cellular metabolic activity, cellular viability, and cell membrane integrity (Fig8. D, E, and F). Importantly, we show that rivaroxaban induced G2-S cell cycle arrest in cultured Plum-AD cells, that was not reversed through PAR-2 agonism (Fig9. G).

We next assessed the potential of rivaroxaban to induce oxidative stress in cultured Plum-AD cells. Indeed, we show that rivaroxaban treatment was associated with increased DHE staining and enhanced ROS generation evidenced by markedly reduced NBT (Fig9. A, B, and C). It is worth noting that while PAR-2 agonism alone reduced ROS generation beyond basal levels, the combination of rivaroxaban and PAR-2 did not mitigate rivaroxaban-induced surge in ROS (Fig9. C). Similar trends were observed with DHE staining albeit not being significant. Such discordance in the observed effects can probably be attributed to the different sensitivities of both assays measuring cellular ROS. Moreover, we did not detect significant alteration of mitochondrial membrane potential evidenced by no change of Mitotracker Orange staining across the experimental conditions (Fig9. A and D).

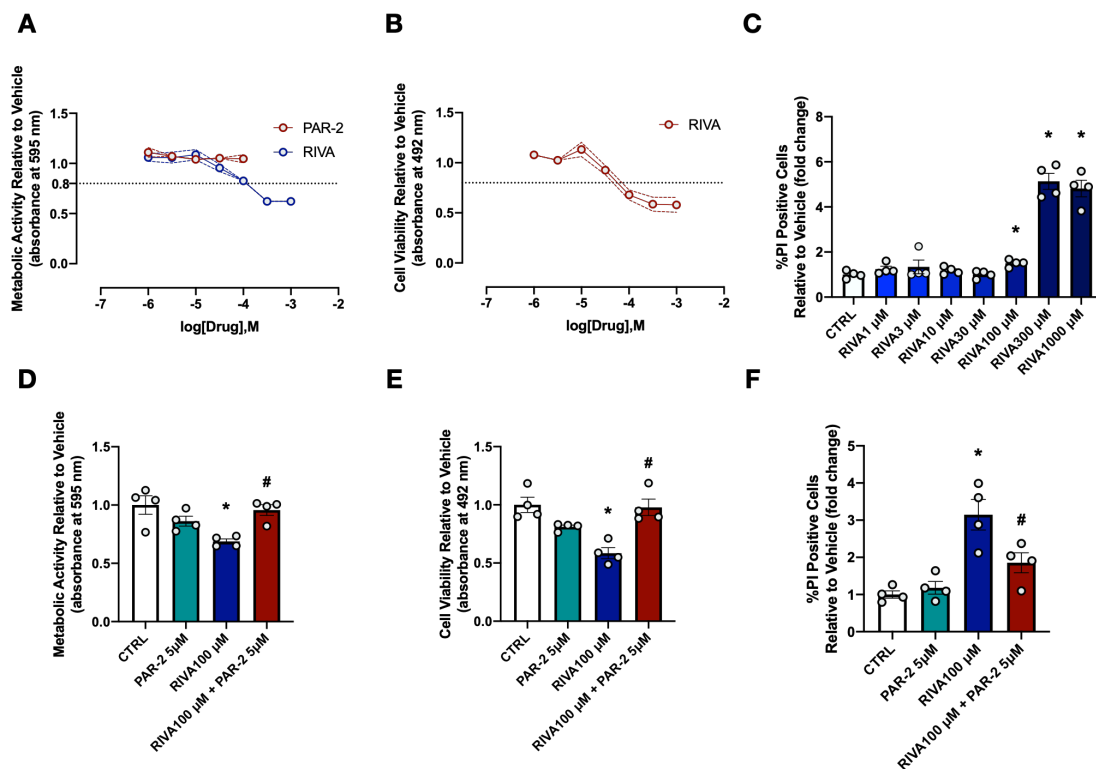


**Figure 8. PAR-2 agonism mitigates rivaroxaban-induced cytotoxicity in cultured murine Plum-AD prostate cancer cells**

**A**, MTT assay assessing cellular metabolic activity in response to increasing concentrations of rivaroxaban (n=6) and PAR-2 (n=4). **B**, SRB assay evaluating cellular viability in response to increasing concentrations of rivaroxaban (n=4). **C**, Fold change of %PI positive cells in response to increasing concentrations of rivaroxaban (n=4). **D**, MTT assay assessing cellular metabolic activity in response to rivaroxaban, PAR-2, and their combination (n=4). **E**, SRB assay evaluating cellular viability in response to rivaroxaban, PAR-2, and their combination (n=4). **F**, Fold change of %PI positive cells in response to rivaroxaban, PAR-2, and their combination (n=4). Values are Mean  $\pm$  S.E.M. Statistical significance was tested using one-way ANOVA followed by Tukey's multiple comparisons (p-value<0.05). \* denotes significance when comparing to the CTRL group while # denotes significance when comparing the RIVA group.

We also investigated the inhibitory effects of rivaroxaban on Plum-AD cellular migration and colony formation potential. Rivaroxaban was shown to significantly reduce cellular migration in the presence or absence of PAR-2 (Fig9. E and F). Rivaroxaban treatment also significantly inhibited Plum-AD colony formation in the presence or absence of PAR-2 (Fig9. H and I). Notably, PAR-2 agonism alone had no effects on Plum-AD cellular migration or colony formation potential.

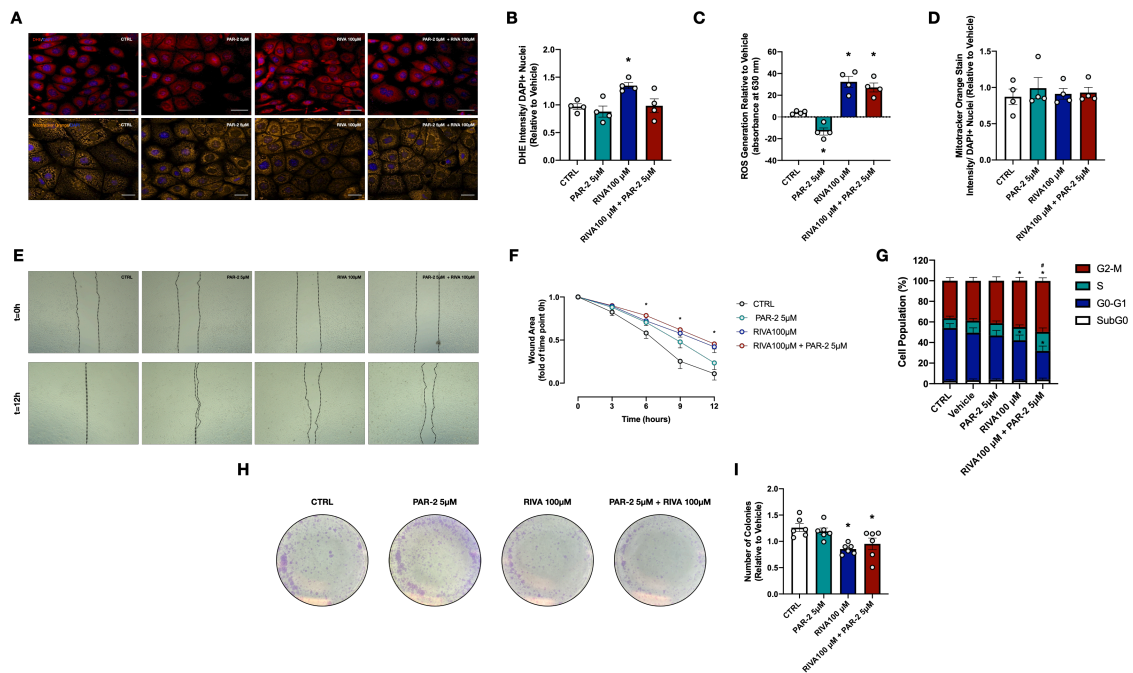


**Figure 9. PAR-2 agonism does not reverse rivaroxaban-induced inhibition of Plum-AD cell migration and colony formation**

**A**, Representative images depicting DHE and Mitotracker Orange-stained Plum-AD cells. **B**, Quantification of Plum-AD DHE stain. **C**, Quantification of NBT reduction indicative of cellular ROS production. **D**, Quantification of Plum-AD Mitotracker Orange stain. **E**, Representative images depicting Plum-AD cell migration at t=0 and t=12 timepoints. **F**, Quantification of Plum-AD cell migration. **G**, Cell cycle quantification depicting cell population percentages belonging to different cell cycle phases. **H**, Representative images of Plum-AD colony formation assay. **I**, Quantification of Plum-AD colony formation. Values are Mean  $\pm$  S.E.M. Statistical significance was tested using one-way ANOVA followed by Tukey's multiple comparisons or two-way ANOVA followed by Sidak's multiple comparisons test ( $p$ -value $<0.05$ ). \* denotes significance when comparing to the CTRL group while # denotes significance when comparing the RIVA group.

## CHAPTER V

### DISCUSSION

Despite the longstanding appreciation of metabolic dysfunction-associated PCa development, progression, and worse prognosis, the molecular underpinnings of such an association have not been elaborately studied (4). Emerging evidence highlights the contribution of PPAT expansion, dysfunction, and inflammation in states of metabolic disturbance in the development, progression, response to chemotherapy, and prognosis of PCa (14-17, 79). Particularly, correlations between PPAT thickness/volume and BMI have yielded inconsistent results (26), and obesity was recently shown not to augment PPAT inflammation and fibrosis (25). As such, it becomes plausible that this discordance of epidemiological data derives from the lack of metabolic characterization of obesity. This highlights the need for rigorous metabolic profiling of patients prior to biopsying. As such, we have utilized a non-obese, prediabetic rat model that is characterized by IR, hypertriglyceridemia, increased adiposity, and localized adipose tissue inflammation in the absence of hyperglycemia, hypertension, and systemic inflammation (70-72, 80).

We have shown that the development of prediabetes is associated with pronounced PPAT adipocyte hypertrophy, augmented oxidative stress, and increased inflammation. Consistent with clinical data on PPAT of PCa patients with obesity (29), we observed the accumulation of pro-inflammatory macrophages encircling hypertrophic adipocytes, forming CLSs in prediabetic rats. Particularly, PPAT was shown to exhibit an intrinsic hypoxic phenotype (25), that is possibly instigated by PPAT adipocyte hypertrophy, reduced PPAT vascular density, and impaired pro-angiogenic response in our model. We suggest that PPAT inflammation is mainly driven by infiltrating M1-polarized macrophages as we did not detect increased PPAT mast cell infiltration. In spite



of the growing interest in PPAT thermogenic potential (81), we failed to detect changes in PPAT sympathetic innervation and adipocyte beta3 adrenergic receptor expression. This could be explained by the early nature of our model's metabolic insult. Nevertheless, this does not exclude the possible thermogenic potential of PPAT and its modulatory effect on the prostate.

Metabolic disturbances culminating in insulin resistance, metabolic syndrome, and obesity are associated with a hypercoagulable state (26). Likewise, cancer creates a highly prothrombotic state evidenced by cancer-associated venous thromboembolism (56). Anticoagulants are incorporated into treatment regimens of cancer patients to counteract such thromboembolic events (57, 58). Importantly, it was shown that chronic treatments with conventional anticoagulants are associated with reduced incidence of certain cancers (60, 61). This is of particular interest as components of the coagulation cascade, particularly thrombin and FXa drives PCa development and progression, partially through their proteolytic activities on PARs (59). Moreover, increased thrombin and FXa activity evidenced by enhanced adipose tissue fibrin deposition drives adipose tissue inflammation (64). We have detected enhanced fibrin deposition in the PPAT, which is a surrogate of increased PPAT FXa activity. We propose that this enhanced FXa activity in the PPAT promotes primitive prostatic neoplasia in our rat model of mild metabolic dysfunction. As such, a two-week rivaroxaban treatment of MHC-fed rats ameliorated IR and reduced serum insulin levels. This was associated with reduced PPAT dysfunction evidenced by reduced adipocyte hypertrophy, oxidative stress, fibrin deposition, macrophage infiltration, and ameliorated pro-angiogenic response. However, rivaroxaban treatment did not interfere with PPAT-infiltrating macrophage polarization. It is worth mentioning that the pharmacological inhibition of thrombin activity through

the anticoagulant drugs dabigatran and argatroban reduces adipose tissue inflammation and protects mice from diet-induced obesity (64, 66-68). Moreover, the inhibition of PAR-2 signaling was also protective against diet-induced obesity and adipose tissue inflammation (52). Therefore, we propose that rivaroxaban-mediated amelioration of PPAT dysfunction in MHC diet-fed rats primarily stems from reduced adipocyte hypertrophy and fibrin deposition-induced adipose tissue macrophage infiltration as previously shown (64). We also suggest that these effects are possibly secondary to reduced PPAT adipocyte PAR-2 signaling.

In association with PPAT dysfunction, prediabetic rats exhibited prostates with increased PIN formation, epithelial thickness, and intraluminal epithelial cell infiltration consistent with models of diet-induced PCa (28). We detected no alteration of acinar luminal diameter which indicates the absence of a developmental prostatic pathology and argues that the observed prostatic structural alterations are secondary to metabolic dysfunction. Indeed, MHC-fed rats exhibited pronounced fibrosis, oxidative stress, mast cell and M1-polarized macrophage infiltration. These prostatic morphological and functional alterations were reversed by rivaroxaban treatment. Moreover, rivaroxaban did not alter prostate-infiltrating macrophage polarization. Although these ameliorative effects of rivaroxaban on the prostate cannot be fully attributed to the amelioration of PPAT dysfunction, we speculate that this is partially the case. We also propose that these ameliorations might also derive from direct effects of rivaroxaban on the prostate.

MHC-fed rats exhibited prostates with hyperproliferative epithelial cells and increased epithelial basal-to-luminal migration. This was associated with enhanced expression of the proliferation markers ki67 and PCNA and the transcription factors Slug and Snail which drive epithelial cell migration and EMT. The latter is evidenced by

enhanced vimentin but not  $\alpha$ -SMA expression relative to CK8. This is consistent with previous findings showing enhanced prostatic basal-to-luminal migration and EMT in high fat diet-fed mice (82). Importantly, rivaroxaban treatment reduced the prostatic epithelial expression of ki67, PCNA, and vimentin suggesting that rivaroxaban inhibits prostatic epithelial migration and EMT. Although we cannot rule out direct effects of rivaroxaban on prostatic epithelial cells, we suggest that rivaroxaban-mediated inhibition of prostatic epithelial cells migration and EMT is partially due to the amelioration of PPAT dysfunction. Indeed, it was previously shown that obese PPAT-conditioned media enhances PCa cell proliferation and migration *in vitro* (32). Moreover, PPAT adipocytes were shown to direct PCa cell migration in an obesity-dependent manner through a CCL7-CXCL12/CCR3-CXCR4-CXCR7 signaling axis (33, 34). PPAT-induced PCa cell invasion was also suggested to be secondary to NOX5-induced ROS generation and the activation of the HIF1/MMP14 signaling axis (35). PPAT secreted TGF- $\beta$  also enhances PCa cell migration (38). Importantly, FXa-cleaved PAR-2 is known to transactivate TGF receptor signaling, which is suggested to enhance PCa cell migration (26). As such, it becomes plausible that the increased FXa activity observed in PPAT of prediabetic rats promotes prostatic epithelial cell migration through the activation of PAR-2.

We also attempted to explain the molecular mechanisms by which rivaroxaban modulates PCa cell proliferation, migration, and colony formation. We show that rivaroxaban inhibited cellular proliferation and caused G2-M cell cycle arrest at a concentration of 100 $\mu$ M. Although PAR-2 agonism reversed rivaroxaban-induced cytotoxicity, we observed no effect of PAR-2 agonism on rivaroxaban-induced cell cycle arrest suggesting that rivaroxaban-mediated cytotoxicity is not secondary to the observed cell cycle arrest. Moreover, the absence of the induction of cell cycle progression

probably stems from the short duration of PAR-2 treatment. As such, we cannot exclude a more advanced pro-mitogenic effect of PAR-2 on Plum-AD cells. PAR-2 agonism was also shown to reduce basal ROS levels as was previously shown in colonic epithelial cells (83). Nevertheless, PAR-2 agonism failed to reverse rivaroxaban-induced ROS production in cultured Plum-AD cells suggesting that rivaroxaban-enhanced ROS generation is independent of its inhibition of PAR-2 cleavage by FXa. The mechanisms by which rivaroxaban induces ROS production in PCa cells requires further investigation. We had similar observations on Plum-AD cellular migration and colony formation, where PAR-2 agonism failed to rescue rivaroxaban-induced inhibition of PCa cell migration and colony formation potential. As such, we propose that rivaroxaban acts through a plethora of signaling pathways including the inhibition of PAR-2 signaling, to modulate PCa cell behavior *in vitro*. The identification of such molecular mechanisms are pivotal in understanding how PPAT thromboinflammation and the associated prostatic neoplastic alterations could be modulated by currently available anticoagulant drugs.

Collectively, we provide a framework by which mild metabolic dysfunction-induced PPAT dysfunction drives early prostatic neoplastic alterations and propose that a myriad of the observed pathological phenomena are secondary to PAR-2 activation among other mechanisms to be investigated. We also propose that rivaroxaban, partially through the inhibition of PAR-2 signaling, halts prostatic neoplastic alterations secondary to metabolic dysfunction. There currently exists no consensus on the anticoagulant therapy of PCa patients and as such, we believe that the pleiotropic effects of rivaroxaban on the PPAT and the prostate warrants further investigation to guide future therapies.

## CHAPTER VI

### LIMITATIONS AND FUTURE DIRECTIONS

The present study has several limitations. First, the safety profile of rivaroxaban dose and the anticoagulant side effects resulting in non-thromboembolic disorders have not been evaluated in rats and thus an exact non-hemorrhagic dose eliciting the above described effects cannot be directly inferred. Nevertheless, we have utilized a rivaroxaban dose that we already showed exhibited an anti-inflammatory activity in other adipose depots including the perivascular and the perirenal adipose depots (84, 85). Moreover, and although we speculate that rivaroxaban ameliorative effect on the PPAT and the prostate were downstream of PAR-2 signaling inhibition, the causality between enhanced PAR-2 signaling and PPAT dysfunction-associated prostatic neoplasia cannot be confirmed from the presented data. The implication of this pathway in the *in vivo* prediabetic rat model we studied requires further investigation. Another limitation is presented by the lack of control groups either put on fructose water for the last two weeks of rearing or put on fructose water and treated with rivaroxaban for the last two weeks of rearing. As such, we cannot exclude rivaroxaban-induced effects in non-metabolically impaired rats. Although we used fibrin deposition as a surrogate for enhanced FXa activity in the PPAT and speculated that PPAT-derived FXa drove the observed prostatic manifestations, we currently are unable to validate such a speculation. Ongoing coculture and adipocyte-conditioned media experiments will provide such insights. Lastly, we have utilized PIN-derived Plum-AD cancer cells as a convenient model of our observed *in vivo* manifestations. The utilization of primary prostatic epithelial cells constitute a more relevant model for this study.

## REFERENCES

1. Siegel RL, Miller KD, Fuchs HE, Jemal A. Cancer statistics, 2021. *CA: a cancer journal for clinicians*. 2021;71(1):7-33.
2. Control CfD, Prevention. National diabetes statistics report: estimates of diabetes and its burden in the United States, 2014. Atlanta, GA: US Department of Health and Human Services. 2014;2014.
3. Care D. Economic costs of diabetes in the US in 2012. 2013.
4. Lavalette C, Trétarre B, Rebillard X, Lamy P-J, Cénée S, Menegaux F. Abdominal obesity and prostate cancer risk: epidemiological evidence from the EPICAP study. *Oncotarget*. 2018;9(77):34485.
5. Pillon NJ, Loos RJ, Marshall SM, Zierath JR. Metabolic consequences of obesity and type 2 diabetes: Balancing genes and environment for personalized care. *Cell*. 2021;184(6):1530-44.
6. Santoro A, McGraw TE, Kahn BB. Insulin action in adipocytes, adipose remodeling, and systemic effects. *Cell Metabolism*. 2021;33(4):748-57.
7. Lee YS, Kim J-w, Osborne O, Sasik R, Schenk S, Chen A, et al. Increased adipocyte O<sub>2</sub> consumption triggers HIF-1 $\alpha$ , causing inflammation and insulin resistance in obesity. *Cell*. 2014;157(6):1339-52.
8. Herold J, Kalucka J. Angiogenesis in Adipose Tissue: The Interplay Between Adipose and Endothelial Cells. *Frontiers in Physiology*. 2021:1861.
9. AlZaim I, Hammoud SH, Al-Koussa H, Ghazi A, Eid AH, El-Yazbi AF. Adipose tissue immunomodulation: a novel therapeutic approach in cardiovascular and metabolic diseases. *Frontiers in Cardiovascular Medicine*. 2020;7:277.
10. Hildreth AD, Ma F, Wong YY, Sun R, Pellegrini M, O'Sullivan TE. Single-cell sequencing of human white adipose tissue identifies new cell states in health and obesity. *Nature immunology*. 2021;22(5):639-53.
11. Sárvári AK, Van Hauwaert EL, Markussen LK, Gammelmark E, Marcher A-B, Ebbesen MF, et al. Plasticity of epididymal adipose tissue in response to diet-induced obesity at single-nucleus resolution. *Cell Metabolism*. 2021;33(2):437-53. e5.
12. Vijay J, Gauthier M-F, Biswell RL, Louiselle DA, Johnston JJ, Cheung WA, et al. Single-cell analysis of human adipose tissue identifies depot-and disease-specific cell types. *Nature metabolism*. 2020;2(1):97-109.
13. Bäckdahl J, Franzén L, Massier L, Li Q, Jalkanen J, Gao H, et al. Spatial mapping reveals human adipocyte subpopulations with distinct sensitivities to insulin. *Cell metabolism*. 2021;33(9):1869-82. e6.
14. Estève D, Roumigué M, Manceau C, Milhas D, Muller C. Periprostatic adipose tissue: A heavy player in prostate cancer progression. *Current Opinion in Endocrine and Metabolic Research*. 2020;10:29-35.
15. Liotti A, La Civita E, Cennamo M, Crocetto F, Ferro M, Guadagno E, et al. Periprostatic adipose tissue promotes prostate cancer resistance to docetaxel by paracrine IGF-1 upregulation of TUBB2B beta-tubulin isoform. *The Prostate*. 2021;81(7):407-17.
16. Mangiola S, Stuchbery R, McCoy P, Chow K, Kurganovs N, Kerger M, et al. Androgen deprivation therapy promotes an obesity-like microenvironment in periprostatic fat. *Endocrine connections*. 2019;8(5):547-58.
17. Kapoor J, Namdarian B, Pedersen J, Hovens C, Moon D, Peters J, et al. Extraprostatic extension into periprostatic fat is a more important determinant of prostate

- cancer recurrence than an invasive phenotype. *The Journal of urology*. 2013;190(6):2061-7.
18. Ishidoya S, Endoh M, Nakagawa H, Saito S, Arai Y. Novel anatomical findings of the prostatic gland and the surrounding capsular structures in the normal prostate. *The Tohoku journal of experimental medicine*. 2007;212(1):55-62.
  19. Kiyoshima K, Yokomizo A, Yoshida T, Tomita K, Yonemasu H, Nakamura M, et al. Anatomical features of periprostatic tissue and its surroundings: a histological analysis of 79 radical retropubic prostatectomy specimens. *Japanese journal of clinical oncology*. 2004;34(8):463-8.
  20. Reeves F, Battye S, Borin JF, Corcoran NM, Costello AJ. High-resolution map of somatic periprostatic nerves. *Urology*. 2016;97:160-5.
  21. Ganzer R, Stolzenburg J-U, Wieland WF, Bründl J. Anatomic study of periprostatic nerve distribution: immunohistochemical differentiation of parasympathetic and sympathetic nerve fibres. *European Urology*. 2012;62(6):1150-6.
  22. Hong H, Koch MO, Foster RS, Bihrlé R, Gardner TA, Fyffe J, et al. Anatomic distribution of periprostatic adipose tissue: a mapping study of 100 radical prostatectomy specimens. *Cancer: Interdisciplinary International Journal of the American Cancer Society*. 2003;97(7):1639-43.
  23. Miladinovic D, Cusick T, Mahon KL, Haynes A-M, Cortie CH, Meyer BJ, et al. Assessment of periprostatic and subcutaneous adipose tissue lipolysis and adipocyte size from men with localized prostate cancer. *Cancers*. 2020;12(6):1385.
  24. Ribeiro R, Monteiro C, Silvestre R, Castela A, Coutinho H, Fraga A, et al. Human periprostatic white adipose tissue is rich in stromal progenitor cells and a potential source of prostate tumor stroma. *Experimental biology and medicine*. 2012;237(10):1155-62.
  25. Roumigué M, Estève D, Manceau C, Toulet A, Gilleron J, Belles C, et al. Periprostatic Adipose Tissue Displays a Chronic Hypoxic State that Limits Its Expandability. *Am J Pathol*. 2022.
  26. AlZaim I, Al-Saidi A, Hammoud SH, Darwiche N, Al-Dhaheri Y, Eid AH, et al. Thromboinflammatory Processes at the Nexus of Metabolic Dysfunction and Prostate Cancer: The Emerging Role of Periprostatic Adipose Tissue. *Cancers*. 2022;14(7):1679.
  27. Kwon O-J, Zhang B, Zhang L, Xin L. High fat diet promotes prostatic basal-to-luminal differentiation and accelerates initiation of prostate epithelial hyperplasia originated from basal cells. *Stem cell research*. 2016;16(3):682-91.
  28. Narita S, Nara T, Sato H, Koizumi A, Huang M, Inoue T, et al. Research evidence on high-fat diet-induced prostate cancer development and progression. *Journal of Clinical Medicine*. 2019;8(5):597.
  29. Gucalp A, Iyengar NM, Zhou XK, Giri DD, Falcone DJ, Wang H, et al. Periprostatic adipose inflammation is associated with high-grade prostate cancer. *Prostate cancer and prostatic diseases*. 2017;20(4):418-23.
  30. Miyazawa M, Subbaramaiah K, Bhardwaj P, Zhou XK, Wang H, Falcone DJ, et al. Pioglitazone inhibits periprostatic white adipose tissue inflammation in obese mice. *Cancer Prevention Research*. 2018;11(4):215-26.
  31. Bhardwaj P, Ikeda T, Zhou XK, Wang H, Zheng XE, Giri DD, et al. Supplemental estrogen and caloric restriction reduce obesity-induced periprostatic white adipose inflammation in mice. *Carcinogenesis*. 2019;40(7):914-23.
  32. Ribeiro R, Monteiro C, Cunha V, Oliveira MJ, Freitas M, Fraga A, et al. Human periprostatic adipose tissue promotes prostate cancer aggressiveness in vitro. *J Exp Clin Cancer Res*. 2012;31(1):32.

33. Laurent V, Guérard A, Mazerolles C, Le Gonidec S, Toulet A, Nieto L, et al. Periprostatic adipocytes act as a driving force for prostate cancer progression in obesity. *Nat Commun.* 2016;7:10230.
34. Saha A, Ahn S, Blando J, Su F, Kolonin MG, DiGiovanni J. Proinflammatory CXCL12-CXCR4/CXCR7 Signaling Axis Drives Myc-Induced Prostate Cancer in Obese Mice. *Cancer Res.* 2017;77(18):5158-68.
35. Kapoor J, Namdarian B, Pedersen J, Hovens C, Moon D, Peters J, et al. Extraprostatic extension into periprostatic fat is a more important determinant of prostate cancer recurrence than an invasive phenotype. *J Urol.* 2013;190(6):2061-6.
36. Fontaine A, Bellanger D, Guibon R, Bruyère F, Brisson L, Fromont G. Lipophagy and prostate cancer: association with disease aggressiveness and proximity to periprostatic adipose tissue. *J Pathol.* 2021;255(2):166-76.
37. Laurent V, Toulet A, Attané C, Milhas D, Dauvillier S, Zaidi F, et al. Periprostatic Adipose Tissue Favors Prostate Cancer Cell Invasion in an Obesity-Dependent Manner: Role of Oxidative Stress. *Mol Cancer Res.* 2019;17(3):821-35.
38. La Civita E, Liotti A, Cennamo M, Crocetto F, Ferro M, Liguoro P, et al. Peri-Prostatic Adipocyte-Released TGF $\beta$  Enhances Prostate Cancer Cell Motility by Upregulation of Connective Tissue Growth Factor. *Biomedicines.* 2021;9(11).
39. Lo JC, Clark AK, Ascui N, Frydenberg M, Risbridger GP, Taylor RA, et al. Obesity does not promote tumorigenesis of localized patient-derived prostate cancer xenografts. *Oncotarget.* 2016;7(30):47650.
40. Alaaeddine RA, AlZaim I, Hammoud SH, Arakji A, Eid AH, Abd-Elrahman KS, et al. The pleiotropic effects of antithrombotic drugs in the metabolic–cardiovascular–neurodegenerative disease continuum: impact beyond reduced clotting. *Clinical Science.* 2021;135(8):1015-51.
41. Solli H, Olsen M, Larsen FB, Pedersen L, Schmidt M. Physical Activity as an Effect Modifier of the Association Between Obesity and Venous Thromboembolism: A Danish Population-Based Cohort Study. *Clinical Epidemiology.* 2020;12:1361.
42. Vilahur G, Ben-Aicha S, Badimon L. New insights into the role of adipose tissue in thrombosis. *Cardiovascular research.* 2017;113(9):1046-54.
43. Chitongo P, Roberts L, Yang L, Patel R, Lyall R, Luxton R, et al. Visceral adiposity is an independent determinant of hypercoagulability as measured by thrombin generation in morbid obesity. *TH Open.* 2017;1(02):e146-e54.
44. Kaji N, Nagakubo D, Hashida S-I, Takahashi S, Kuratani M, Hirai N, et al. Shortened blood coagulation times in genetically obese rats and diet-induced obese mice. *Journal of Veterinary Medical Science.* 2013;75(9):1245-8.
45. Godsland I, Crook D, Proudler A, Stevenson J. Hemostatic risk factors and insulin sensitivity, regional body fat distribution, and the metabolic syndrome. *The journal of clinical endocrinology & metabolism.* 2005;90(1):190-7.
46. Raynaud E, Pérez-Martin A, Brun J-F, Aïssa-Benhaddad A, Fédou C, Mercier J. Relationships between fibrinogen and insulin resistance. *Atherosclerosis.* 2000;150(2):365-70.
47. Luyendyk JP, Schoenecker JG, Flick MJ. The multifaceted role of fibrinogen in tissue injury and inflammation. *Blood, The Journal of the American Society of Hematology.* 2019;133(6):511-20.
48. Leurs PB, Stolk RP, Hamulyak K, Van Oerle R, Grobbee DE, Wolffenbuttel BH. Tissue factor pathway inhibitor and other endothelium-dependent hemostatic factors in



- elderly individuals with normal or impaired glucose tolerance and type 2 diabetes. *Diabetes Care*. 2002;25(8):1340-5.
49. Samad F, Pandey M, Loskutoff DJ. Regulation of tissue factor gene expression in obesity. *Blood, The Journal of the American Society of Hematology*. 2001;98(12):3353-8.
  50. Ford ES. The metabolic syndrome and C-reactive protein, fibrinogen, and leukocyte count: findings from the Third National Health and Nutrition Examination Survey. *Atherosclerosis*. 2003;168(2):351-8.
  51. Samad F, Pandey M, Loskutoff DJ. Tissue factor gene expression in the adipose tissues of obese mice. *Proceedings of the National Academy of Sciences*. 1998;95(13):7591-6.
  52. Badeanlou L, Furlan-Freguia C, Yang G, Ruf W, Samad F. Tissue factor–protease-activated receptor 2 signaling promotes diet-induced obesity and adipose inflammation. *Nature medicine*. 2011;17(11):1490-7.
  53. Ay L, Kopp HP, Brix JM, Ay C, Quehenberger P, Scherthaner GH, et al. Thrombin generation in morbid obesity: significant reduction after weight loss. *Journal of Thrombosis and Haemostasis*. 2010;8(4):759-65.
  54. Kopp CW, Kopp HP, Steiner S, Kriwanek S, Krzyzanowska K, Bartok A, et al. Weight loss reduces tissue factor in morbidly obese patients. *Obesity research*. 2003;11(8):950-6.
  55. Lijnen HR, Van Hul M, Hemmeryckx B. Caloric restriction improves coagulation and inflammation profile in obese mice. *Thrombosis research*. 2012;129(1):74-9.
  56. Elyamany G, Alzahrani AM, Bukhary E. Cancer-associated thrombosis: an overview. *Clinical Medicine Insights: Oncology*. 2014;8:CMO. S18991.
  57. Ay C, Beyer-Westendorf J, Pabinger I. Treatment of cancer-associated venous thromboembolism in the age of direct oral anticoagulants. *Annals of Oncology*. 2019;30(6):897-907.
  58. Weitz JI, Chan NC. Novel antithrombotic strategies for treatment of venous thromboembolism. *Blood, The Journal of the American Society of Hematology*. 2020;135(5):351-9.
  59. Cantrell R, Palumbo JS. The thrombin–inflammation axis in cancer progression. *Thrombosis Research*. 2020;191:S117-S22.
  60. Schulman S, Lindmarker P. Incidence of cancer after prophylaxis with warfarin against recurrent venous thromboembolism. *New England Journal of Medicine*. 2000;342(26):1953-8.
  61. Pengo V, Noventa F, Denas G, Pengo MF, Gallo U, Grion AM, et al. Long-term use of vitamin K antagonists and incidence of cancer: a population-based study. *Blood, The Journal of the American Society of Hematology*. 2011;117(5):1707-9.
  62. Kohli M, Williams K, Yao JL, Dennis RA, Huang J, Reeder J, et al. Thrombin expression in prostate: a novel finding. *Cancer investigation*. 2011;29(1):62-7.
  63. Heuberger DM, Schuepbach RA. Protease-activated receptors (PARs): mechanisms of action and potential therapeutic modulators in PAR-driven inflammatory diseases. *Thrombosis journal*. 2019;17(1):1-24.
  64. Kopec AK, Abrahams SR, Thornton S, Palumbo JS, Mullins ES, Divanovic S, et al. Thrombin promotes diet-induced obesity through fibrin-driven inflammation. *The Journal of clinical investigation*. 2017;127(8):3152-66.

65. Strande JL, Phillips SA. Thrombin increases inflammatory cytokine and angiogenic growth factor secretion in human adipose cells in vitro. *Journal of Inflammation*. 2009;6(1):1-10.
66. Kopec AK, Joshi N, Towery KL, Kassel KM, Sullivan BP, Flick MJ, et al. Thrombin Inhibition with Dabigatran Protects against High-Fat Diet–Induced Fatty Liver Disease in Mice. *Journal of Pharmacology and Experimental Therapeutics*. 2014;351(2):288-97.
67. Feldmann K, Grandoch M, Kohlmorgen C, Valentin B, Gerfer S, Nagy N, et al. Decreased M1 macrophage polarization in dabigatran-treated Ldlr-deficient mice: implications for atherosclerosis and adipose tissue inflammation. *Atherosclerosis*. 2019;287:81-8.
68. Mihara M, Aihara K-i, Ikeda Y, Yoshida S, Kinouchi M, Kurahashi K, et al. Inhibition of thrombin action ameliorates insulin resistance in type 2 diabetic db/db mice. *Endocrinology*. 2010;151(2):513-9.
69. Takahashi N, Yoshizaki T, Hiranaka N, Kumano O, Suzuki T, Akanuma M, et al. The production of coagulation factor VII by adipocytes is enhanced by tumor necrosis factor- $\alpha$  or isoproterenol. *International journal of obesity*. 2015;39(5):747-54.
70. Elkhatib MA, Mroueh A, Rafeh RW, Sleiman F, Fouad H, Saad EI, et al. Amelioration of perivascular adipose inflammation reverses vascular dysfunction in a model of nonobese prediabetic metabolic challenge: potential role of antidiabetic drugs. *Translational Research*. 2019;214:121-43.
71. Hammoud SH, AlZaim I, Mougharbil N, Koubar S, Eid AH, Eid AA, et al. Perirenal adipose inflammation contributes to renal dysfunction in a non-obese prediabetic rat model: Role of anti-diabetic drugs. *Biochemical Pharmacology*. 2021;186:114491.
72. Dwaib HS, Ajouz G, AlZaim I, Rafeh R, Mroueh A, Mougharbil N, et al. Phosphorus Supplementation Mitigates Perivascular Adipose Inflammation–Induced Cardiovascular Consequences in Early Metabolic Impairment. *Journal of the American Heart Association*. 2021;10(24):e023227.
73. Galarraga M, Campión J, Muñoz-Barrutia A, Boqué N, Moreno H, Martínez JA, et al. Adiposoft: automated software for the analysis of white adipose tissue cellularity in histological sections. *Journal of lipid research*. 2012;53(12):2791-6.
74. Selvadurai MV, Moon MJ, Mountford SJ, Ma X, Zheng Z, Jennings IG, et al. Disrupting the platelet internal membrane via PI3KC2 $\alpha$  inhibition impairs thrombosis independently of canonical platelet activation. *Sci Transl Med*. 2020;12(553).
75. Daoud G, Monzer A, Bahmad H, Chamaa F, Hamdar L, Mouhieddine TH, et al. Primary versus castration-resistant prostate cancer: modeling through novel murine prostate cancer cell lines. *Oncotarget*. 2016;7(20):28961.
76. Chaaban I, Hafez H, AlZaim I, Tannous C, Ragab H, Hazzaa A, et al. Transforming iodoquinol into broad spectrum anti-tumor leads: Repurposing to modulate redox homeostasis. *Bioorganic Chemistry*. 2021;113:105035.
77. Choi HS, Kim JW, Cha YN, Kim C. A quantitative nitroblue tetrazolium assay for determining intracellular superoxide anion production in phagocytic cells. *J Immunoassay Immunochem*. 2006;27(1):31-44.
78. Hanahan D. Hallmarks of cancer: new dimensions. *Cancer discovery*. 2022;12(1):31-46.
79. Alzaim I, Darwiche N, Abou-kheir W, El-Yazbi AF. Periprostatic Adipose Tissue Thromboinflammation Drives Early Prostatic Neoplastic Alterations in a Rat Model of Mild Metabolic Dysfunction. *The FASEB Journal*. 2022;36.

80. Fakh W, Mroueh A, Salah H, Eid AH, Obeid M, Kobeissy F, et al. Dysfunctional cerebrovascular tone contributes to cognitive impairment in a non-obese rat model of prediabetic challenge: role of suppression of autophagy and modulation by anti-diabetic drugs. *Biochemical Pharmacology*. 2020;178:114041.
81. Álvarez-Artime A, García-Soler B, Sainz RM, Mayo JC. Emerging roles for browning of white adipose tissue in prostate cancer malignant behaviour. *International Journal of Molecular Sciences*. 2021;22(11):5560.
82. Kwon OJ, Zhang B, Zhang L, Xin L. High fat diet promotes prostatic basal-to-luminal differentiation and accelerates initiation of prostate epithelial hyperplasia originated from basal cells. *Stem Cell Res*. 2016;16(3):682-91.
83. He L, Ma Y, Li W, Han W, Zhao X, Wang H. Protease-activated receptor 2 signaling modulates susceptibility of colonic epithelium to injury through stabilization of YAP in vivo. *Cell death & disease*. 2018;9(10):1-11.
84. Al-Saidi AM, Abdallah S, Hammoud S, Mougharbil N, El-Yazbi A. Interruption of Perirenal Adipose Tissue Thromboinflammation Reverses Prediabetic Kidney Impairment. *Circulation*. 2021;144(Suppl 1):A10233-A.
85. AL Arab G. POSSIBLE CONTRIBUTION OF PERI-VASCULAR ADIPOSE THROMBO-INFLAMMATION TO CARDIAC AUTONOMIC NEUROPATHY: MODULATION BY RIVAROXABAN 2021.